The Astrophysical Journal Supplement Series, 139:259–279, 2002 March

MOUNT WILSON SYNOPTIC MAGNETIC FIELDS: IMPROVED INSTRUMENTATION, CALIBRATION, AND ANALYSIS APPLIED TO THE 2000 JULY 14 FLARE AND TO THE EVOLUTION OF THE DIPOLE FIELD

Roger K. Ulrich, Scott Evans, John E. Boyden, and Larry Webster
Department of Physics and Astronomy, University of California, Los Angeles, CA 90095
Received 2001 March 31; accepted 2001 October 9

ABSTRACT

This paper describes the current status of the 150 foot solar tower telescope program of synoptic observations with an emphasis on the magnetic field data. A newly installed 24-channel system permits routine intercomparison of magnetic fields measured by the λ676.8 nm line used by the Michelson Doppler Imager (MDI) on the *Solar and Heliospheric Observatory* and the λ525.0 nm line used by the 150 foot tower. Two important calibration procedures for treatment of saturation and zero-point offset are described. It is demonstrated that solar rotation can be used to extract the east-west component of the slowly evolving, large-scale magnetic field in a stable fashion. This same analysis produces maps of the neutral line configurations that are well correlated with the positions of quiescent prominences. The analysis is applied to the 2000 July 14 flare and shown to demonstrate that the field was sheared due to the westward-moving intrusion of a region just north of the neutral line along which the flaring occurred. A new method for preparing synoptic charts by averaging without differential rotation smearing is presented. These synoptic charts are combined into a new format termed a supersynoptic chart, which makes possible the identification of systematic long-term trends in the magnetic field evolution. Based on these charts, distinct large-scale events of magnetic field bias opposing the old-cycle dipole field are seen. A statistical method using the skewness in the distribution of the polarity bias as a function of longitude is developed. The coincidence between pulses in this skewness and times of rapid change in the Sun's dipole moment is consistent with the idea that a tilt in the orientation of bipolar magnetic regions is responsible for the dipole field reversal. The pulses in skewness are large and limited in number, suggesting the operation of a large-scale instability such as the kink instability.

Subject headings: Sun: activity — Sun: magnetic fields — Sun: prominences

1. INTRODUCTION

Routine monitoring of the Sun's magnetic field is an essential resource for understanding the solar dynamo. The synoptic program of magnetic and velocity measurements carried out at the 150 foot solar tower telescope of the Mount Wilson Observatory maintains such a program (hereafter referred to at the 150 foot tower program). This paper describes recent improvements to the data taking and data analysis systems of the 150 foot tower program. These aspects of the 150 foot tower program include implementation of a new 24-channel data-taking system, correction of the field strength for saturation effects, resolution of the vector field into two components, and a modification to the algorithm used to prepare synoptic charts.

A primary objective of the 150 foot tower program is to improve our understanding of the solar cycle whose magnetic field variation over a 22 year interval is generally accepted to be the consequence of a dynamo process. The generation and/or amplification of the magnetic field in a dynamo is the result of rotation and convection in a magnetized plasma. The mathematical description of a dynamo starts from a combination of the induction equation and the hydrodynamic equations. Recent reviews of the dynamo problem are available from Hoyng (1994) and Gilman (2000). Following the ideas of Parker (1955, 1993), such authors as Rüdiger & Brandenburg (1995), Charbonneau & MacGregor (1997), and Dikpati & Charbonneau (1999) roughly reproduce the global properties of the Sun's magnetic cycle with what are called mean-field interface dynamo models. Although there are some successes, considerable areas of difficulty remain. For example, Markiel & Thomas (1999) have shown that the model by Charbonneau & MacGregor (1997) is a result of an unphysical boundary condition. The primary figure of merit in evaluating solar dynamo models is a comparison between model and solar magnetic field butterfly diagrams that require the proper periodicity of field reversal and latitude migration of the sunspots. It is noteworthy that this comparison is only at the level where solar properties have been averaged and smoothed considerably and not at a level where significant details about the solar magnetic distribution are retained. Section 9 of this paper defines a longitudinal contribution function for the magnetic field and shows that this contribution function provides a valuable measure of the process that generates the dipole reversal. The time dependence of the skewness of this contribution function suggests a nonsteadiness in the field reversal process.

The numerical models leading to the theoretical butterfly diagrams include parameters that are adjusted to achieve agreement with the observed butterfly diagrams. In one type of model, the parameters are denoted by α and β, where α represents the rate of magnetic field generation through the helicity of the turbulent velocity field and β represents an eddy viscosity that causes the mean field to decay. These parameters were introduced by Steenbeck & Krause (1969) and elaborated upon by Krause & Rädler (1980), who showed that the Coriolis force acting on rising and expanding convective currents produces a cyclonic motion that generates helicity in the field configuration and eventually allows for regeneration of large-scale magnetic fields. A similar effect can be produced through the numerical modeling of rising magnetic flux tubes as the Coriolis force twists them and produces Joy's law of sunspot tilt (Gilman & Howard 1986). Models based on this approach were first introduced by Babcock (1961) and elaborated on by Leighton (1969). These more heuristic models are able to reproduce greater detail in the magnetic evolution than is the case with the more formal mean field, interface models (Wang, Sheeley, & Nash 1991). The skew in the field distribution introduced in § 9 is a global indicator of this twisting process that may be useful as a test of the heuristic models.

The synoptic monitoring of the Sun's magnetic field is useful for predicting the near-term state of solar activity. Conditions in interplanetary space and in the near-Earth space environment are estimated according to methods developed by Wang and Sheeley (Wang & Sheeley 1990, 1995a, 1995b). These are now used on a real-time basis to forecast the solar wind speed and magnetic field direction at Earth.[1] This approach is based on a potential field model connecting the solar surface to a source surface at 2 $R_{\odot}$. The use of potential field models is described by Altshuler and Newkirk (1969), Wang & Sheeley (1992), and Zhao & Hoeksema (1993, 1995) for the model connecting the solar surface to the solar wind source surface. This latter surface provides the interface boundary condition for the interplanetary medium and knowledge of the magnetic field on this surface allows the prediction of the solar wind speed (Wang & Sheeley 1990, 1995a, 1995b). The operational applications of this model are described by Zhao & Hoeksema (1993) and Arge & Pizzo (2000). One of the reduction steps (the treatment of a saturation effect) described below is carried out on the Mount Wilson data prior to its use in the operational models. This step was described only briefly by Ulrich (1992) and is described here in greater detail.

The vector nature of the magnetic field requires acquisition of a full set of linear and circular polarization measurements in order to permit a complete description of the state of solar magnetism. The knowledge of the full state of the solar magnetic field is required to evaluate the deviation of the field from a potential form or a force-free form. It is known from studies by Hagyard et al. (1984) that the stress involved with nonpotential fields and shear can be used to estimate the stability of various structures. The magnetic components transverse to the line of sight can be measured directly only through a reliable measurement of the linear polarization of the sunlight. Vector magnetograph systems are in routine operation at several observatories: the Mees Solar Observatory (Mickey 1985), the Huairou station of the Beijing Astronomical Observatory (Wang et al. 1996), and the US National Solar Observatory with the Advanced Stokes Polarimeter (Lites et al. 1995). Because of a variety of instrumental effects, the transverse magnetic field must be strong (typically 100–150 G) before the induced linear polarization can be reliably measured. Consequently, the monitoring of the weak large-scale solar magnetic field is carried out by means of the measurement of circular polarization that yields only the line-of-sight component of the Sun's magnetic field. Section 6 below shows how the stationary east-west component of the Sun's transverse magnetic field can be estimated using the variable viewing due to solar rotation.

In this paper we report several improvements to the Mount Wilson 150 foot tower synoptic program that enhance the value of the observations in addressing the questions of the solar dynamo and in diagnosing the near-real-time state of the Sun's magnetic field. The particular improvements we have made are the following:

1. We have increased the number of spectral channels from four to 24 so that we can simultaneously measure the velocities and magnetic field for four different spectral lines and so that we can use multiple parts of the spectral lines. This system makes it possible to closely match the observing system used by the Michelson Doppler Imager (MDI) helioseismology instrument on the *Solar and Heliospheric Observatory* (*SOHO*). The multiple channels also permit the study of the altitude dependence of the magnetic field and doppler velocities.
2. We now introduce correction into some of our data products for the effects of spectral line saturation. A scale based on λ523.3 nm is adopted as a saturation-independent reference. Except for the evaluation of the Sun's dipole moment in § 9, none of the results presented in this paper have been corrected for the saturation effect.
3. A method for finding the magnetic zero-point shift due to mirror polarization effects is described and used to compute synoptic charts that compare the positions of magnetic neutral lines to the locations of quiescent prominences.
4. A method of compensating for differential rotation in the construction of magnetic maps averaged over multiple observations is described. Without this technique, the superposition of observations of a single portion of the solar surface but taken at times that differ by more than a few hours would produce a smearing of the average image.
5. The method of Shrauner & Scherrer (1994) is applied in concert with the position adjustment to permit a resolution of the stationary part of the magnetic field into two components, one in the east-west direction and the other a projection onto the meridional plane. This magnetic field geometry information is presented in the form of a tilt map that may be useful in estimating the stability of magnetic configurations.

These methods are used to prepare a set of sample synoptic charts that show excellent agreement between the positions of the magnetic neutral lines and the quiescent prominences. In particular, the standard assumption of a vertical photospheric magnetic field is seen to be inconsistent with the tilt maps that show persistent east-west tilts to the magnetic field over most of the solar surface. The method is applied to the 2000 July 14 flare and is shown to reveal shear structures in the flaring regions.

The magnetic fields reduced according to these new procedures show a stability that makes it useful to consider the long term evolution of global measures of the field including its lowest order magnetic moment: its dipole strength. As a step to understanding the largest scale averages, we combine the resulting synoptic charts for a period of just over 6 years into a format we term a supersynoptic chart. This chart is used to discuss the process of field reversal, which is a central part of the dynamo action. The tilt that places the trailing sunspot poleward of the leading spot can be seen on a global scale using the supersynoptic chart. In order to quantify this effect, a statistical description of the magnetic field distribution is developed based on the dipole moment contribution of each longitudinal strip. The integral of these over a full rotation gives the dipole moment. The variance and skewness of the distribution function for these contri-

[1] See http://sec.noaa.gov/~narge/.

butions provide measures of the strength of the bipolar magnetic regions and their contribution to the axial dipole moment, respectively. The skewness is shown to correspond to the temporal rate of change of the axial dipole moment.

2. THE 24-CHANNEL SPECTROPHOTOMETER SYSTEM

Starting in 1996, the Mount Wilson 150 foot tower telescope system began using a new 24-channel spectral sampling system. The large astronomical grating in use in the pit spectrograph of this system has 367.5 grooves mm^{-1}, is blazed at 60°, and operates simultaneously in orders 7–9. This grating replaced the older 632 groove mm^{-1} grating that had operated in the fifth-order green. The telescope/spectrograph is unusual by modern standards in that the only optics are the two-mirror coelostat, the objective lens, an image slicer, the camera/collimator lens, and the grating. This simple geometry combined with the thermally stable pit configuration yields a system with very little spectrograph seeing. Since the f/ratio of 150 is preserved throughout the system, the image scale is large at the final spectrograph focus, and the final detector element must also be large. Solid-state detectors with large geometry have high noise and dark current that would degrade the data quality compared to what is possible using a photometric approach.

The system operates in a fashion similar to that described by Howard et al. (1983). Four sets of fiber-optic image reformators similar to those shown in Figure 1 of Howard et al. (1983) extract slices of the solar spectrum and redirect the light to two new assemblies, each of which has 12 photomultiplier tubes. The four reformator bundles are centered on the lines $\lambda525.02$ and $\lambda523.72$ nm, the Na D line at $\lambda589.59$ nm, and the line of Ni at $\lambda676.79$ nm. The entrance face of each bundle has a dimension of about 5×28 mm^2, which is divided into 20 slender rectangles of size about 0.25×28 mm^2. The long dimension of the rectangles is oriented parallel to the spectral lines in the cross-dispersion direction, thus slicing the spectrum into sections with a minimal spread in wavelength acceptance. Each rectangular slice of fiber bundle is reconfigured into a circular output that is directed onto the photocathode of the photomultiplier tube. These rectangles are packed next to each other with a clean boundary between each so that when the solar spectrum falls onto the entrance end, it is separated into a set of spectrally pure slices. The system utilizes four sets of these reformators: two having 20 input/output bundles, one having 10, and one having seven. The 10-bundle fiber has been in use since 1988 to observe $\lambda523.7$ nm. The other three sets were acquired in 1995 to work with the 24-channel system. The new seven-bundle set closely matches the spectral sampling with the older diffraction grating that operated in fifth order at $\lambda525.0$ nm.

The photometer assembly with its cover removed is shown in Figure 1, and in Figure 2 the same assembly is shown with its covers on and with a fiber-optic image reformator attached. The attached reformator is the older 10-slice one that is now in use for $\lambda523.7$ nm. It is shown here attached to the red stage where one of the newer 20-slice assemblies is in use. Note that the output faces are used in groups of two to extend the spectral coverage of $\lambda676.8$ nm. The underlying hardware setup could be configured to use all 20 slices independently in order to provide more detail in the line profile. This alternative would come at the cost of the other line that is now studied with the second new 20-slice reformator, Na D_1.

Since there are a total of 37 fiber bundles available but only 24 photomultiplier/electronic channels that can be used, the bundles have to be either grouped together or some of them have to be left without a detector. Both strategies are used. For $\lambda523.7$ nm, only two bundles are used. For $\lambda525.0$ nm, the seven-bundle unit is used and the bundles are combined in groups of three, with the one in the middle being left without a detector. For $\lambda589.6$ nm, one of the new 20 bundle sets is used. In this case 10 of the bundles are capped off and the other 10 are sent singly to separate photomultipliers in these combinations: two as far out on the line as possible and two pairs that bracket the working point of the Global Oscillations at Low Frequencies (GOLF) instrument on *SOHO* (Gabriel et al. 1995). Finally, for $\lambda676.8$ nm, all bundles are used and their outputs are combined in pairs. This permits a complete coverage of this line so that the filtergram observing system of the MDI instrument on *SOHO* can be simulated (Scherrer et al. 1995). All of these configurations are shown in Figure 3. We note that this system allows for future science program modification by the simple reconfiguration of the spectral line sampling.

The 24-channel detector system is divided into two banks of 12 channels, each of which is carried on a moveable stage. The stage on the blue side carries the fiber-optic entrance ends for $\lambda523.7$ and $\lambda589.6$ nm, while the red stage carries the entrance ends for $\lambda525.0$ and $\lambda676.8$ nm. Following the Babcock magnetograph strategy, the position of each of these combined fiber-optic plus photomultiplier tube assemblies is dynamically adjusted during the observation so that the intensities of the photomultipliers of one pair are equalized. Normally for the blue and red stages, respectively, the feedback signal comes from the intermediate channels on $\lambda589.6$ and $\lambda525.0$ nm.

The system operation is very similar to what was described by Howard et al. (1983). In particular, the 400 Hz repeat frequency has been retained. The integration process is based on this rate. Each half-cycle of 0.00125 s then defines an integration time for the system that we refer to as the KD*P half-cycle time. A data set for each area of the Sun is then the sum of a large number of these KD*P half-cycle integrations, with there being 48 numbers per area (two for each channel) integration. The system digitization begins with a preamplifier that produces a voltage proportional to the light intensity striking the photocathode of the photomultiplier. This voltage is converted to a stream of pulses by means of a voltage-to-frequency converter. The pulses produced by this converter are summed in a local active register for each photomultiplier tube (PMT). At the end of each KD*P half-cycle, all of the active registers transfer their values to a holding register and the active register is cleared. While the KD*P crystal is changing its state, the storage registers transfer their results serially to the control computer where they are organized for recording onto the data tape.

3. CORRECTION FOR THE SATURATION EFFECT

The effect described in this section consists of a multiplicative correction factor, which brings to a common scale the apparent line-of-sight magnetic field strength as measured by different spectral line sampling pairs. This correction fac-

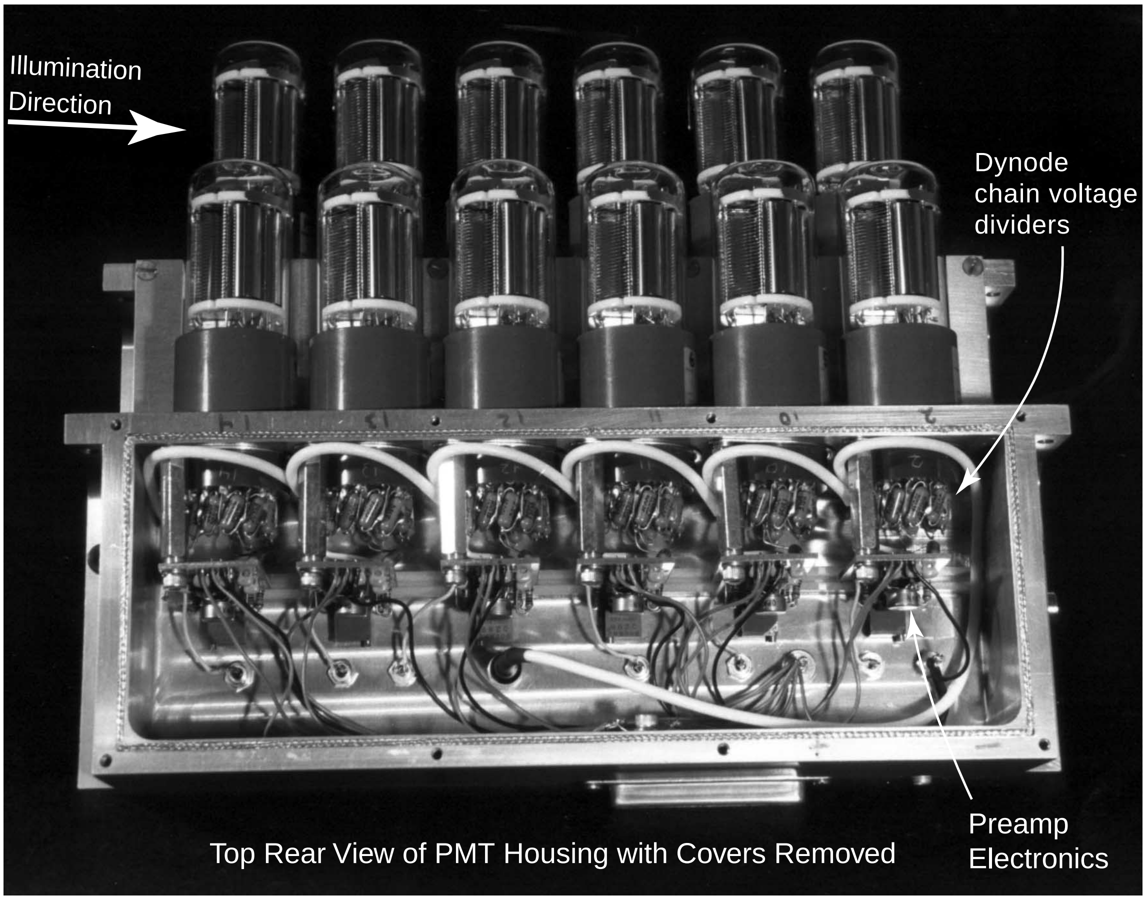

FIG. 1.—Red PMT stage with its covers removed to illustrate the internal components. The preamplifier electronics are closely coupled to the PMT mounting fixture. The covers are sealed with an antiradio frequency interference gasket to eliminate the adverse effects of the TV transmission towers near the Mount Wilson observatory.

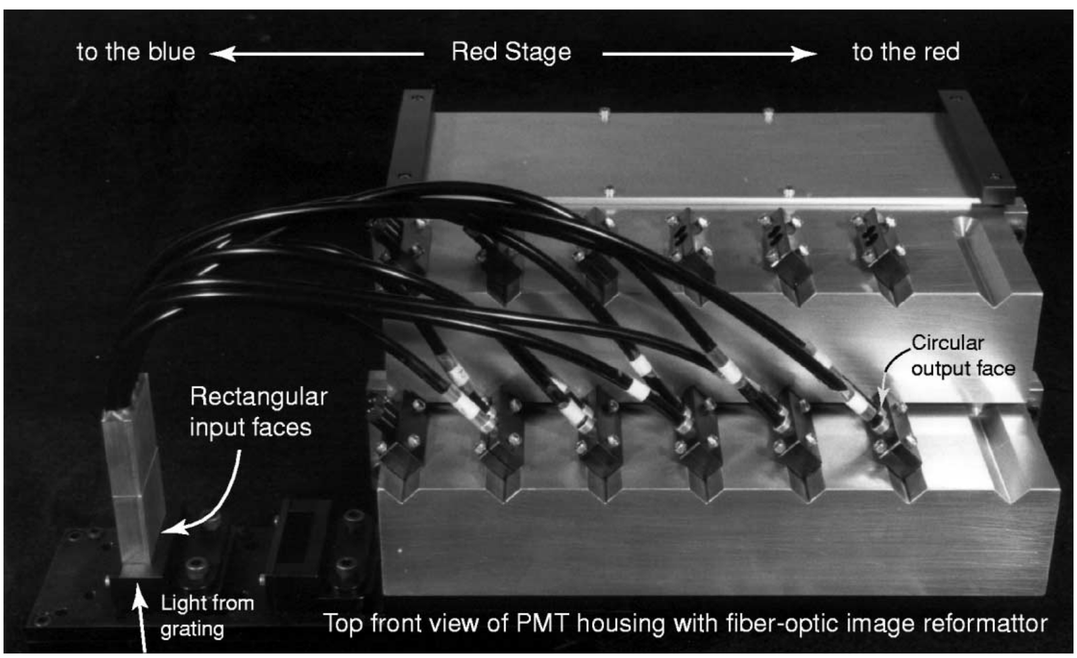

FIG. 2.—Red PMT stage with its covers on and with an illustrative configuration for a fiber-optic image reformator attached. Light from the spectrograph enters from below. There are now order separation filters installed below each entrance face.

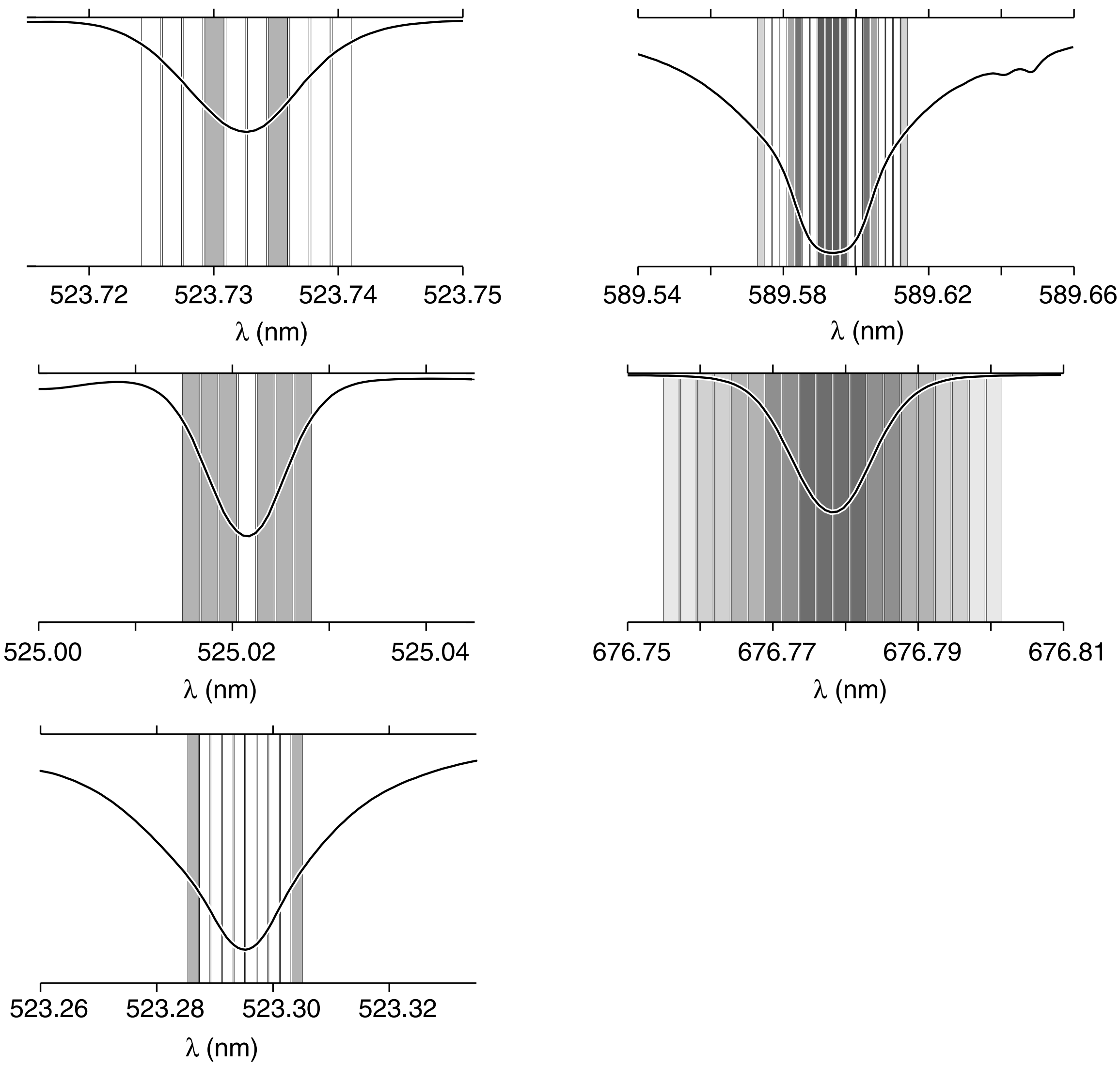

FIG. 3.—This figure shows the spectral line profiles as provided by the archives of the US National Solar Observatory. The sampling bandpass is shown by the sets of rectangles plotted behind the line profiles. Each rectangle represents the spectral sampling wavelength range and has a circular output that may or may not be directed into a photomultiplier tube so that the radiation intensity can be measured. Those rectangles that are white are not used. The gray rectangles are combined so that red- and blue-wing pairs with the same density of gray form a set that can be used in the standard Babcock magnetograph mode.

tor should be used for studies of global field models but has not been applied to any of the photospheric fields as reported in this paper or in earlier papers from the 150 foot tower synoptic program. It will be explicitly stated when and if results reported by this program are modified by this correction factor.

3.1. *The Flux Tube Model*

Solar magnetic fields are known to have a highly inhomogeneous structure consisting of strong-field flux tubes embedded in a plasma that is only weakly magnetized if at all (Spruit, Schüssler, & Solanki 1991). A range of flux tube structure has been explored by Steiner & Pizzo (1989), and one specific model presented by Steiner (1994) is used here as a representative case. The relationship between the flux tube structure and the height of formation of the spectral lines measured with the Mount Wilson system are shown in Figure 4. Circular polarization in the spectral-line wings comes from the Zeeman effect, which shifts the spectral line by a wavelength displacement that is large compared to the spectral sampling of the Mount Wilson 150 foot tower system. When the Zeeman shift moves the line core blueward of the red edge of the blue passband and redward past the blue edge of the red passband, the net circular polarization in each band can no longer respond to a magnetic field increase because as much radiation is gained on the trailing edge of the passband as is lost at the leading edge. This condition represents a saturation of the magnetograph. The actual deduced magnetic field, then, is responding to the fill factor rather than the magnetic field itself. Most spectral lines used for magnetic and Doppler measurements are subject to this saturation effect for at least some parts of their profile. Because of temperature and line transfer influences, line profiles are sensitive to magnetic fields, so any large scale measurement represents a complex average over the fields that are present in the sampled area. Outside of sunspot regions, the net result of these effects is for the fill factor to be the dominant factor so that all apparent magnetic fields are proportional to each other with different constants

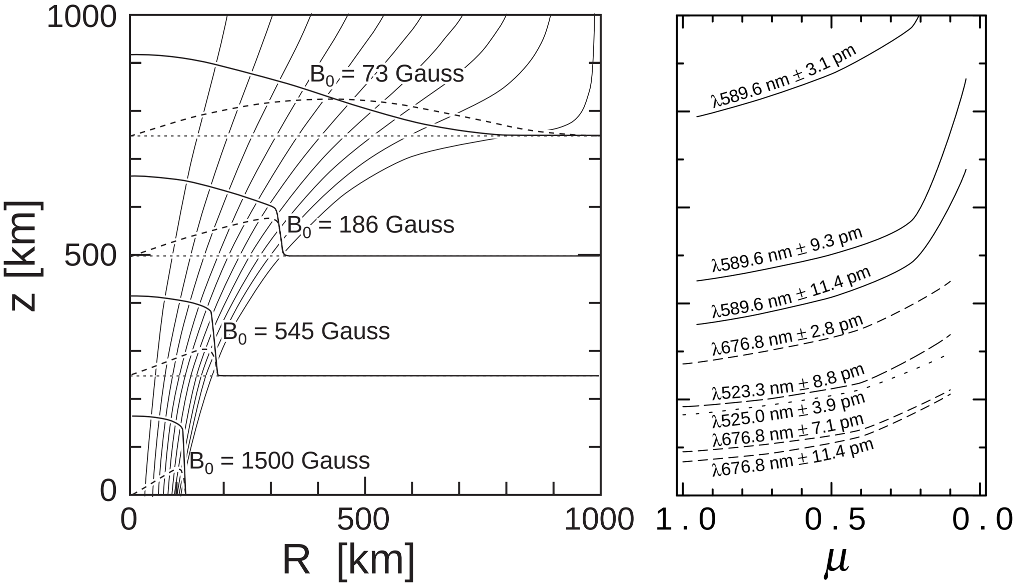

FIG. 4.—Left figure is adapted from Fig. 6 in the review by Steiner (1994). The magnetic structure of the tube is given at four equally spaced altitudes. For the upper three field plots the zero level is shown as the short-dashed line, the vertical field strength is shown as the solid line, and the transverse field is shown as the long-dashed line. The fields are scaled so that the vertical field strength on the axis has the value given as B_0. The right figure shows the heights of formation (G. Severino 1996, private communication; L. Bertello 2000, private communication; Caccin et al. 1977) as a function of μ, the cosine of the center-to-limb angle. Each line is labeled with its central wavelength in nanometers (nm) along with the half-separation between the red and blue bandpasses in picometers (pm). Lines having the same central wavelength are drawn with the same style of dashed or solid lines. Both the flux tube model and the heights of formation are indications rather than precise quantities. The flux tube has a specific base strength of 1500 G at an altitude of 100 km and is modeled to be in a region where it merges with its neighbor where the typical distance between flux tube centers is 2000 km.

of proportionality. The tight correlation between fields measured with different lines with a proportionality different from unity led Howard & Stenflo (1972), Frazier & Stenflo (1972), and Stenflo (1973) to formulate the currently accepted model in which inhomogeneous fields are required.

Since the flux tube magnetic field is a strong function of altitude, the saturation is also a function of altitude, so we can expect the constant of proportionality to depend on the center to limb angle. Outside of sunspot regions there is no indication that this effect depends on any parameter other than the center-to-limb angle and the aperture size for the sampling of the solar surface. No dependence of this saturation factor on solar latitude (other than center-to-limb angle) or on phase of the solar cycle has been detected. A discussion of this effect as applied to the measurements at Mount Wilson was given by Ulrich (1992).

3.2. *Saturation Measurements*

The spectral bandpass selection for the magnetograph at the Mount Wilson 150 foot tower is set by fiber-optic image reformators, as shown in Figure 3. It is clear that the inner edges of the sampling bands for λ525.0 nm are so close to the line core that even a very weak field is sufficient to cause saturation. The inner edges cause saturation effects to occur whenever the solar magnetic field is in excess of 200 G. Although we would choose a different configuration if we were initiating a new synoptic program, we have retained this sampling in order to remain consistent with the historic database that starts in 1967. Other saturation field strengths are higher, but many are still small enough that some correction factors will be necessary. For the useful combinations of input faces, Table 1 gives the magnetic field at which the Zeeman splitting shifts the central wavelength past the inner edge of the sampled bandpass. These values indicate the relative sensitivity of each spectral line sampling pair to the saturation effect.

3.3. *Magnetic Field Comparison*

In order to evaluate the saturation effect and its center-to-limb dependency we use the comparison line at λ523.3 nm shown on the bottom left of Figure 3. As is shown in Table 1, the passbands are spaced widely enough that saturation effects do not occur until the solar field is in excess of 3800 G, which is large enough that even strong flux tubes will not be affected (see Fig. 4). We take the field measured by the λ523.3 nm samples to be the reference and derive from it a correction factor to be applied to λ525.0 nm. For unmerged flux tubes, the vertical magnetic structure is governed primarily by the balance between magnetic and gas pressures. Thus, as the total pressure drops, the tube expands laterally, and the magnetic field strength drops. This effect by itself would not cause a change in the apparent magnetic field because the product of the magnetic field strength and its area is conserved so that changes in the field strength would be compensated for by a change in the fill factor.

Under the flux tube picture the variations in the apparent magnetic field on the solar surface come from variations in the density of these elemental flux tubes—i.e., a variable fill factor is the only cause for variation of the apparent field strength over the solar surface. Whenever different spectral samplings are compared, the primary differences come from the differences in altitude of line formation and from differences in line intensity factors. Because of the compensation between fill factor and magnetic field strength, if these factors were independent of wavelength within a spectral line and were the same for different spectral lines, the apparent magnetic field would be determined uniquely. The actual

TABLE 1
SPECTRAL LINE SAMPLE PAIRS

λ Center (nm)	$\Delta\lambda$ (pm)	B_{Sat} (G)
523.295	8.96[a]	3782[a]
523.733	2.56	790
525.022	0.97	200
589.594	3.14	1920
589.594	9.31	3841
589.594	11.39	4804
676.778	2.82	290[b]
676.778	7.11	4084
676.788	11.45	7636

[a] Values of separations for this line are based on the older dispersion from the 632 line grating in fifth order.

[b] This value is nominally zero since it applies to adjacent entrance apertures. It is listed as 25% of the entrance aperture width.

apparent magnetic field depends on the spectral sampling, however, because the line intensity depends on the field strength and because the Zeeman splitting at the altitude where each part of the line is formed can shift the line in the magnetized portion of the fluid past the saturation point of the spectral passband. The latter effect is what is classically referred to as the saturation effect. That part of the apparent magnetic field variation coming from the variable fill factor can be determined by comparing the apparent fields as measured by separate spectral line sample pairs. In a plot of one field against the other, the slope of a regression line through the scatter plot gives the ratio of the two constants that multiply the fill factor. In addition, a change in the center-to-limb angle ρ corresponds to a change in the altitude of line formation, so we can expect the slopes to be dependent on ρ. This slope has been given the symbol δ^{-1} by Howard & Stenflo (1972), but the symbol ϵ^{-1} is used here to avoid confusion with notation introduced in § 9 below.

Because of the design of the multichannel at the Mount Wilson 150 foot tower spectrograph, it is possible to obtain exactly simultaneous magnetograms. The 400 Hz cycle of the polarimetry system is governed by the voltage oscillation on the KD*P cell, which applies equally to all spectral samples. Thus, all of the wavelength samples are integrated over the same state of image motion induced by atmospheric smearing and can be directly compared. It is much more difficult but nonetheless possible to compare these samples to measurements taken by a different instrument such as MDI in its magnetograph mode. Such comparisons will be done in a subsequent report.

In order to evaluate the relationship between different spectral line sample pairs, the two lines have to be observed simultaneously. As indicated above, the line at λ523.3 nm is well suited to having low-saturation effects and is formed in a similar range of altitude as that of our standard line λ525.0 nm. During the normal synoptic program at the 150 foot tower, however, the line λ523.3 nm is not observed. Consequently, a special configuration with just these two spectral line sample pairs was used on 1991 June 29 and 30. At this time there were only two spectral line sample pairs available, and a lower dispersion spectrograph configuration was in use (note that the configuration appropriate to that period is shown in Fig. 3). Each spatiotemporal pixel that forms the magnetogram thus provided a pair of apparent magnetic fields that can be plotted as a point on the plane of the two magnetic field strengths. Figure 5 shows the distribution of all such points for the pair of lines from λ525.0 and λ523.3 nm for four ranges in ρ. Implementations of the correction factor have been made by Wang & Sheeley (1995a) and Snodgrass, Kress, & Wilson (2000). The slope of the line is given in Table 2 for this pair of spectral samples as well as for three samples from λ676.8 nm. The quantities given in Table 2 are in the sense that they multiply the magnetic field as observed with the listed spectral line sample pairs in order to make it equivalent to that which would have been obtained with λ523.3 nm. Unless explicitly stated otherwise, the magnetic field values given in other sections of this paper have *not* been corrected by these factors. The quantities given for λ676.8 nm were derived from a comparison to λ525.0 nm and then converted to the λ523.3 nm basis by using the comparison of λ525.0 to λ523.3 nm.

For the case of the MDI line, λ676.8 nm, the comparison shown in Table 2 is only indicative since the actual filter system involves a complex average over the whole spectral line. In addition, the detailed tuning of the MDI filter components depends on time during the operations of *SOHO* and on the position on the solar disk due to small filter-dependent factors. Consequently, the kind of detailed analysis required to put the MDI magnetograms on the λ523.3 nm scale is beyond the scope of the present paper.

4. ADJUSTMENT OF THE MAGNETIC ZERO POINT

A Babcock-type magnetograph system provides a magnetic measurement that is largely insensitive to instrumentally induced polarization effects. Because the line-of-sight magnetic field is determined from a double difference of the fractional degree of circular polarization on opposite spectral line wings, most of these polarization artifacts taken one at a time cancel out of the magnetic field determination. However, the combination of two or more imperfections simultaneously can induce spurious magnetic signals. We can detect such effects through, for example, the diurnal drift of the integral of the magnetic signal over the full solar disk. In order to limit the influence of such effects, we have developed a new system for removing the bulk of the instrumental drifts using an assumption about the distribution of weak fields.

We start with the supposition that small-scale convective effects are able to modify the magnetic field through a local tangling process that can produce equal areas of field of opposite sign, at least when integrated over the full solar disk. In order to exploit this assumption, we start by defining and computing a distribution function $\phi(B)$, which gives the fraction of the solar surface area, $\Delta A/A$, covered by fields between B and $B + \Delta B$ as

$$\frac{\Delta A}{A} = \int_{B}^{B+\Delta B} \phi(B) dB \ . \qquad (1)$$

The values recorded for the magnetic field are a combination of the solar field and an error of measurement. As long as the error of measurement is smaller than the width of the

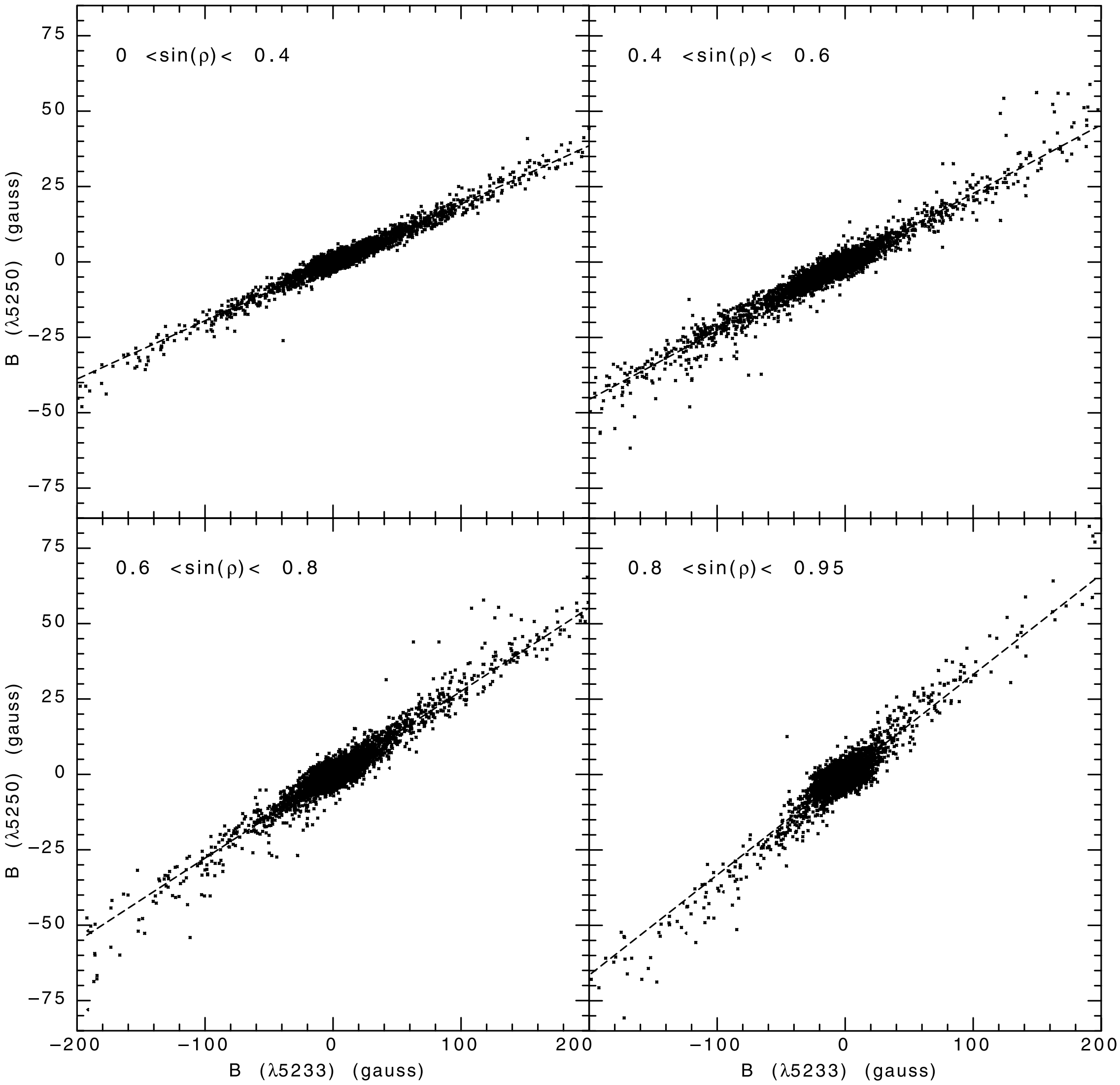

FIG. 5.—Scatter diagrams for the magnetic field measured by the two spectral line sample pairs for a magnetogram having an entrance aperture of 12×12 arcsec^2.

distribution function for solar fields, the actual zero of the magnetic fields should correspond to the point where $\phi(B)$ is a maximum.

The Babcock magnetograph provides four intensities for each spectral line sampling pair defined according to Howard et al. (1983) as A1, A2, B1, and B2, where A and B designate the blue- and red-line wing spectral line samples, and 1 and 2 designate the phase of the selected circular polarization. These four intensities are added and/or subtracted to create four equivalent parameters I, Z, E, and C, where Z/I is essentially the Stokes V parameter, E/I is a measure of the Doppler error, and C/I is a measure of the circular polarization introduced by the telescope with its coelostat mirrors. Based on these quantities we utilize the histogram peak assumption by determining the distribution function for the Z/I parameter, $\phi(Z/I)$, defined analogously to the above formula and then applying an additive adjustment to Z/I to all points so that the peak of the distribution function is at $Z/I = 0$. The magnetic fields are then determined by multiplying the corrected, observed values of Z/I by an appropriate scale factor that depends on the spectral line slope and the effective Zeeman splitting factor, g.

TABLE 2
SATURATION FACTORS

Center-to-Limb Angle	$\cos(\rho)_{\rm Ave}$	525.0 nm ± 1.0 pm	676.8 nm ± 2.8 pm	676.8 nm ± 7.1 pm	676.8 nm ± 11.4 pm
$0.00 < \sin(\rho) < 0.30$	0.980	4.32	2.55	2.65	1.82
$0.30 < \sin(\rho) < 0.55$	0.890	4.00	2.52	2.41	1.83
$0.55 < \sin(\rho) < 0.70$	0.775	3.59	2.38	2.37	1.92
$0.70 < \sin(\rho) < 0.95$	0.510	2.65	2.20	2.19	2.00

NOTE.—Saturation factors, ϵ^{-1}, needed to bring each line to the basis of 523.3

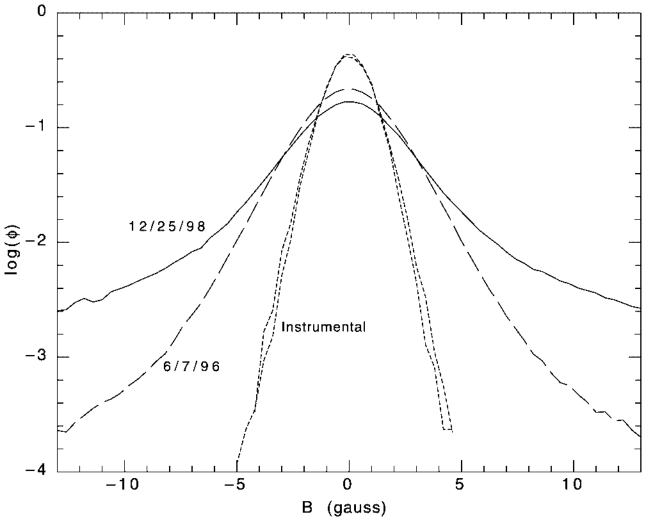

FIG. 6.—Comparison of the instrumental distribution function measured with the circular polarization modulator (the KD*P cell) turned off to the distribution functions measured near solar maximum and solar minimum.

Observed distribution functions at two points of the solar cycle and for the instrumentational error of measurement are shown in Figure 6. This figure demonstrates that the distribution functions are widened by solar effects and that the instrumental effects are not responsible for the observed changes. Furthermore, we can use the measurement of individual, small-scale features by Keller (1993) to determine that the Mount Wilson system is sensitive enough to respond to the addition or subtraction of a single strong flux tube within each pixel. The observed distribution functions confirm that the measurements are sensitive to the small-scale fields produced over the entire solar surface and that our shifting of the circular polarization is appropriate. The zero-point adjustment is important to our ability to determine the locations of the magnetic neutral lines. For the present paper, this adjustment has been done for the data beginning in the year 1996 but has not yet been implemented through a rereduction of the data prior to that time.

5. SYNOPTIC MAP PREPARATION

We have developed a new method of preparing synoptic magnetic charts that permits an accurate representation of the magnetic field. A synoptic chart consists of a mapping of the solar surface onto a coordinate system where the horizontal axis is the Carrington longitude and the vertical axis is the heliographic latitude (or in some cases, the sine of the heliographic latitude). We have multiple observations of each portion of the solar surface during the time for each rotation that the point is visible. The averaging together of the available observations causes smearing due to differential rotation, since the Carrington rotation rate only represents the actual rotation rate at a single latitude. Normally a synoptic chart includes only that data that is on or very near to the Sun's central meridian at the time it was observed. The built-up synoptic map then consists of a sequence of relatively narrow strips along lines of constant longitude. Since only one observation is used per synoptic chart, the noise tends to be higher on a synoptic chart prepared in the traditional manner than could be achieved if several observations were averaged together. In order to carry out averaging without introducing additional smearing, we consider the Carrington coordinates to apply to each point at the time of its central meridian crossing. All other observations are then differentially derotated so that they can be combined at the specified point. The map thus does not represent the solar surface at any fixed time, but rather represents a distorted solar surface where the higher latitudes have been compressed so that their times of central meridian crossing come at regular intervals. If we were to apply this distortion over a long period of time, it would severely alter the solar surface shape. However, since we limit the application to less than one-quarter of a rotation period and reset the zero point for each new rotation, the effect of the high-latitude distortion is minimal. The synoptic maps including the supersynoptic maps reported below have been prepared using the approach described here.

6. EAST-WEST MAGNETIC FIELD LINE TILT

The utility of a vector measurement of the Sun's magnetic field, together with the greater sensitivity of instruments that measure the line-of-sight magnetic field, combine to motivate the use of the Sun's rotation to provide a series of perspective views of a stationary magnetic field. These views can then be used to resolve the magnetic vector into two components, one in an east-west direction and the other in the plane of the Sun's axis of rotation. The latter consists of the vector sum of the component in the north-south direction and the component in the radial direction. Without a true vector magnetograph, there is no way to further resolve these two components. It is nonetheless of considerable interest to make the available resolution of the stationary fields. The earliest use of this concept was by Minnaert (1946), who compared regions on symmetrically placed positions east and west of the central meridian and thus estimated the east-west tilt under the assumption that the field itself was the same in both positions. Similar approaches have been pursued by Howard (1974, 1991, 1994) and Howard & Stanchfield (1995). The principal goal of these works was to determine average field line tilts as a function of latitude. We show here that it is possible to derive magnetic field line tilt maps that may be useful as a diagnostic of magnetic stability.

Our analysis is based on an approach developed by Shrauner & Scherrer (1994), which uses weighted averages of the line-of-sight field to provide the information needed for the vector decomposition. After we have determined the set of derotated points to be combined to form a single synoptic chart point, we can weight the observed values with both the $\sin(L)$ and the $\cos(L)$, where L is the central meridian angle measured negative to the west (note that the field projected in the east-west direction is measured positive to the west). The two magnetic field components we seek can be designated by B_v for the field in the meridional plane and by B_t for the transverse component in the east-west direction. Note that the resolution of the magnetic field into its components must be incomplete for our data because of the fact that we do not obtain an indication of the projection of the field onto the north-south transverse direction. The component designated as B_v is related to the vector field in the manner described in the next section.

6.1. *Definition of the Observable Parameters*

During each solar rotation, a point fixed relative to the differentially rotating coordinate system can be observed I times. We label each measurement of the line-of-sight component of this point on the surface as B_{si} and use weighted averages of these observations to resolve the stationary part of the Sun's magnetic field into the B_v and B_t components. The expression for each B_{si} in terms of B_v and B_t is

$$B_{si} = \cos(L_i) B_v + \sin(L_i) B_t \ . \tag{2}$$

The weighted sums are defined as

$$sb = \sum_i \sin(L_i) B_{si} = sc\, B_v + ss\, B_t \ , \tag{3}$$

$$cb = \sum_i \cos(L_i) B_{si} = cc\, B_v + sc\, B_t \ , \tag{4}$$

where

$$ss = \sum_i \sin^2(L_i) \ , \tag{5}$$

$$sc = \sum_i \sin(L_i)\cos(L_i) \ , \tag{6}$$

$$cc = \sum_i \cos^2(L_i) \ . \tag{7}$$

In terms of these definitions, we may determine the average field components as

$$B_t = \frac{cc\, sb - sc\, cb}{ss\, cc - sc^2} \ , \quad B_v = \frac{ss\, cb - sc\, sb}{ss\, cc - sc^2} \ . \tag{8}$$

After we find the two components of the magnetic field, we can determine a slope angle parameter Ψ, which provides a measure of the east-west deviation of the field line from vertical. This angle Ψ is defined as

$$\tan(\Psi) = \frac{B_t}{B_v} \ . \tag{9}$$

This formula was given by Shrauner & Scherrer (1994), but these authors did not use this to determine a tilt map of the sort we present below because of the low spatial resolution of the data they used from the Wilcox Solar Observatory. In order to limit Ψ so that $-\pi/2 < \Psi < \pi/2$, if $B_v < 0$, we change the sign of both B_t and B_v.

The tilt angle analysis presented here, combined with the magnetic zero-point adjustment described in § 4, allows us to derive the locations of the neutral lines where the vertical magnetic field is zero. Although the tilt angle analysis includes some uncertainties due to the lack of information about the geometry in a north-south direction, the method does take into account the tilt in the east-west direction, which, for arched structures, shifts the location of the neutral line away from disk center in a systematic fashion. It is well known that the quiescent prominences or filaments are found in Hα images above these neutral lines (Hirayama 1985). High-resolution, high time cadence sequences have led to a model in which these structures are identified with a sheared pattern of the magnetic field that overlies the neutral line (Martin & Echols 1994). It is also to be expected that the vertical extension of the neutral line will be associated with a neutral sheet in the coronal regions (Kuperus & Tandberg-Hanssen 1967). Figure 7 sketches these structures schematically, illustrates the relationships between these different features, and shows why the location of the neutral line is shifted away from disk center by the arched structure—the arch line is perpendicular to the line of sight at a point that is closer to the observer than is point where the field line is horizontal.

6.2. *Geometric Interpretation of the Observable Parameters*

A synoptic program of solar magnetic field measurement must include data from the Sun's surface obtained when the point of observation is far from the center of the apparent solar disk. Models of the magnetic field structure above the surface are most conveniently cast in terms of the spherical geometry for the Sun as a whole, such as a global spherical coordinate system of latitude and longitude. Although the Mount Wilson system is not sensitive to the transverse components of the field, they are required to fully describe the field. We start with a coordinate system in which the z-axis is along the line of sight but measured positive outward and the x-axis is in a plane parallel to the solar equator and is in a direction perpendicular to the z-axis. The y-axis completes the orthogonal set conforming to the right-hand rule and lies in the meridional plane but is not tangent to the solar surface. The magnetic field in this system has components B_x, B_y, B_z, where for Mount Wilson only B_z is available. This observable set of components can be converted to spherical components through two rotations—the first about the y-axis and the second about an axis parallel to the equator and tangent to the solar surface.

The first rotation is about the x-axis by an angle b_0, where b_0 is the angle whereby the north pole is tilted toward the observer. This produces a new set of axes x', y', z', for which the y'-axis is parallel to the Sun's axis of rotation but the z'-axis is no longer along the line of sight. The second rotation about the y'-axis by an angle L produces a coordinate system having components $B_{\rm ew}$, $B_{y'}$, B_v where the ew axis is tangent to the solar surface but the v-axis is in the plane parallel to the solar equator and is not normal to the solar surface. The final coordinate system differs from the second by a rotation about the ew axis through an angle of Lat, where Lat is the latitude of the point. The components in this system are $B_{\rm ew}$, $B_{\rm ns}$, B_r. The positive direction for the ew component is toward the west and the positive direction for the ns component is to the north. Figure 8 illustrates some of these angles. The tilt of the magnetic field relative to this final coordinate system is given by two slope angles, $s_{\rm ns}$ and $s_{\rm ew}$, which are illustrated in Figure 8. Note that unlike L, $s_{\rm ew}$ is measured positive when the magnetic field component in the east-west direction is positive. As a convenience we define an additional quantity B_m, which is the projection of the magnetic field onto the local meridional plane having the absolute value satisfying $|B_m|^2 = |B_y|^2 + |B_v|^2 = |B_{\rm ns}|^2 + |B_r|^2$. Taking B to be the absolute value of the field, the two slopes are

$$\sin(s_{\rm ew}) = B_{\rm ew}/B, \quad \sin(s_{\rm ns}) = B_{\rm ns}/B_m \ ;$$
$$\cos(s_{\rm ew}) = B_m/B \ . \tag{10}$$

The observable line-of-sight field B_z is

$$B_z = B\cos(s_{\rm ew})\cos(s_{\rm ns} - {\rm Lat})\cos(L)\cos(b_0) + B\sin(s_{\rm ew})\sin(L)\cos(b_0) + B_{y'}\sin(b_0) \ . \tag{11}$$

The constant term involves the component of magnetic field in the y'-direction, which is parallel to the Sun's axis of rota-

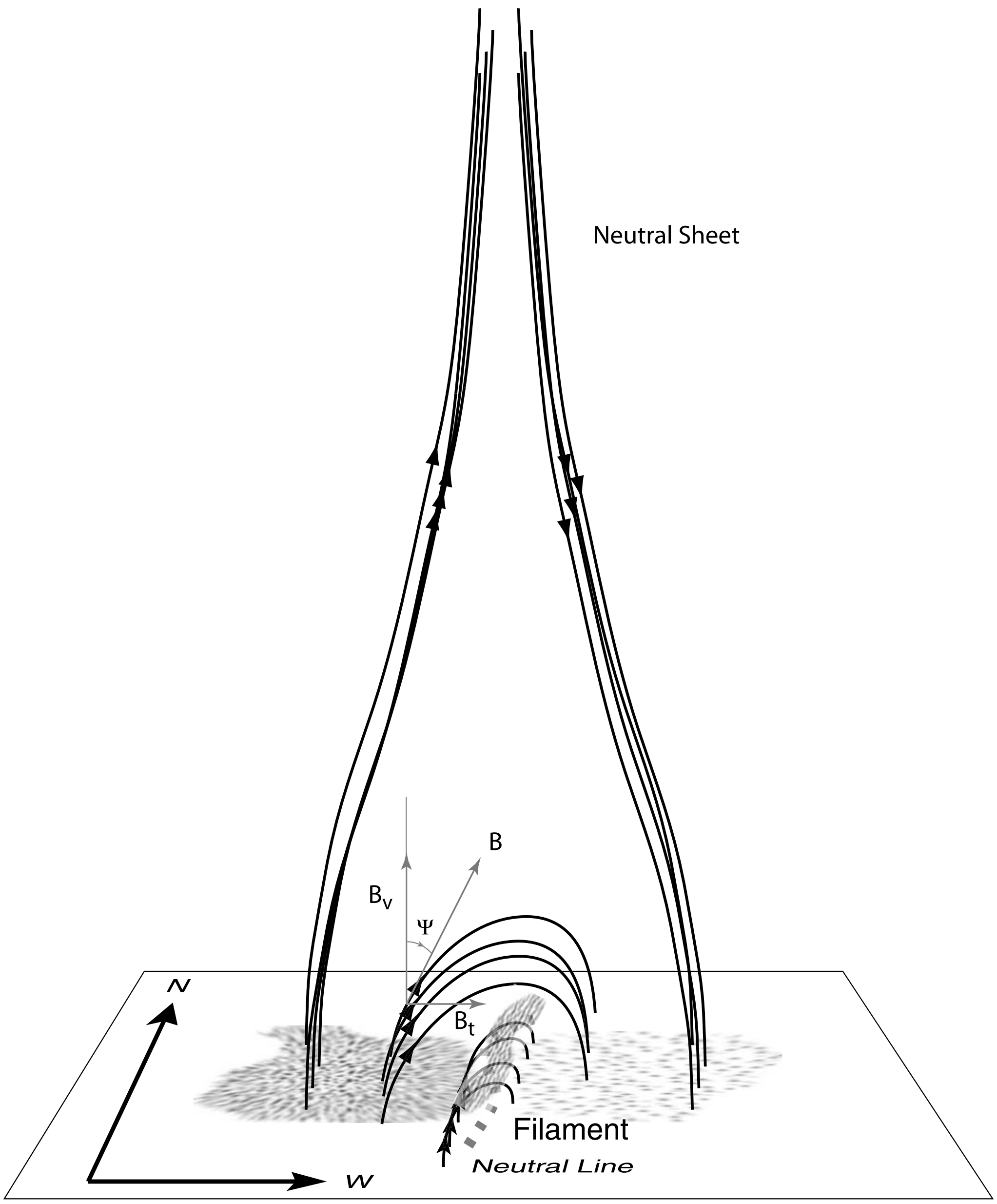

FIG. 7.—Schematic drawing based on the publication by Kuperus & Tandberg-Hanssen (1967) showing adjacent magnetized regions having opposite polarity. The magnetic field lines connect the two regions as shown. The line of magnetic neutrality is shown as the broad dashed line. A neutral sheet is shown above with an associated filament. The two components of field that can be resolved by the method used here are shown as B_v and B_t. Note that the B_v component is the projection of B simultaneously onto the meridional plane and the plane of latitude along the line of sight. That component in the meridional plane but perpendicular to the line of sight is not detected, so the angle calculated from eq. (9) is not the true tilt angle. This issue is discussed further in the following subsection. The angle Ψ shown here is positive, and in Figs. 9, 10, and 11 it is shown as blue. An arch on this figure is represented by a neutral line with blue to the left and red to the right.

tion. Although the correlation analysis approach described in the previous section might be able to estimate this constant term as a zero-point offset, in practice any such estimate is unreliable because of the facts that $\sin(b_0)$ is small and that the time variability of the solar fields reduces any cross-correlation coefficient below unity. It is important to note, however, that this constant offset does not influence the slopes that are used to determine B_v and B_t. Hagyard (1987) gives relationships between vector magnetic field measurements and the field components in the ew, ns, r system, which can be used in global field calculations.

The observational method described in the previous paragraph provides an estimation of $B_t = B_{\rm ew}$ and $B_v = B_m \cos(s_{\rm ns} - {\rm Lat})\cos(b_0)$. The quantity $s_{\rm ew}$, which is the true east-west angle between the plane of the magnetic field and the local meridional plane, is related to the angle Ψ defined above by

$$\tan(\Psi) = \frac{\tan(s_{\rm ew})}{\cos(s_{\rm ns} - {\rm Lat})\cos(b_0)}. \qquad (12)$$

The determination of the east-west field component is not influenced by the uncertainty in the north-south slope. The angle Ψ is a convenient nondimensional indication of the tilt angle of the field in the east-west direction, but we have used a denominator that is influenced by the north-south field

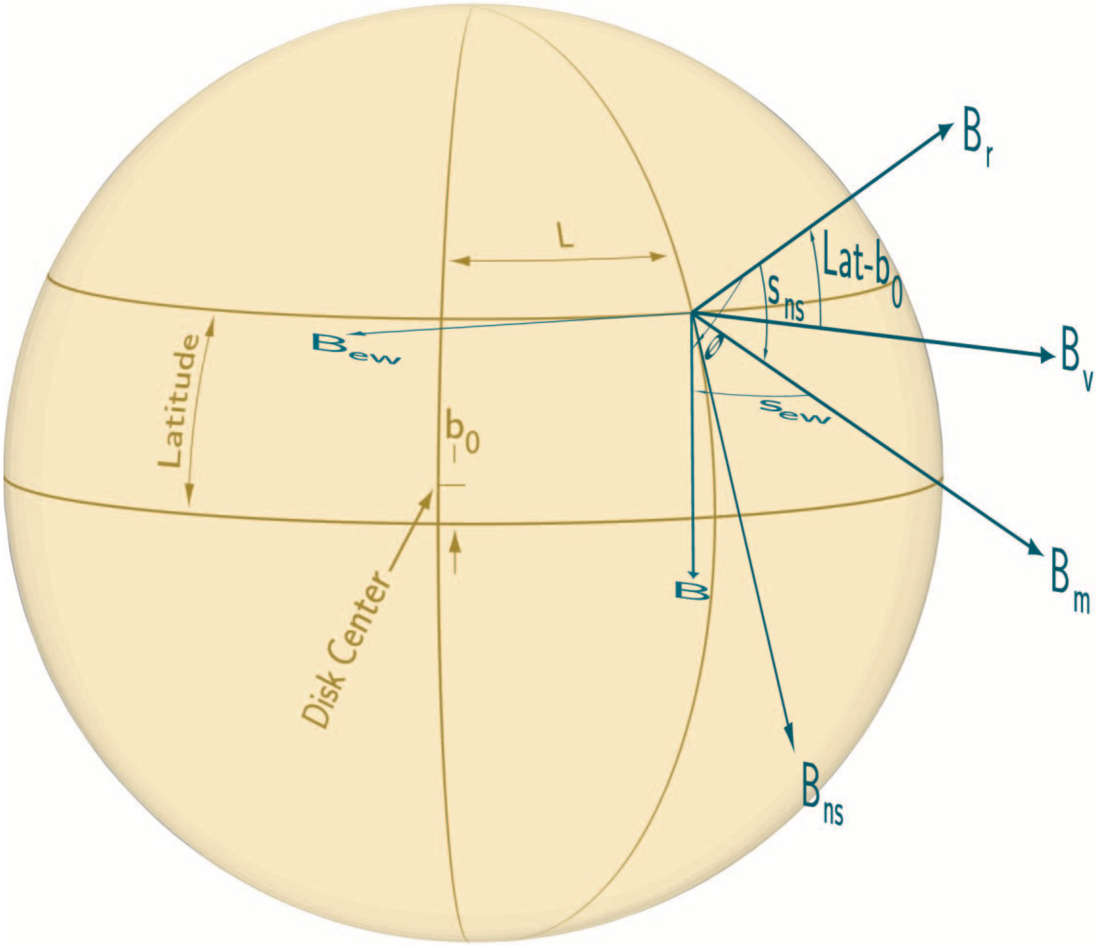

FIG. 8.—Perspective drawing showing the angles relating the observable projections of the magnetic field to those needed to describe the global field. This image is seen from a position 4° west of the central meridian line and from an angle 6° above the equator. The b_0 shown is for $+4\overset{\circ}{.}5$. For clarity of the drawing both $B_{\rm ew}$ and $B_{\rm ns}$ are shown with negative values. The latitude of the point is $+25°$ and the central meridian angle L is $-35°$. The slopes $s_{\rm ew}$, $s_{\rm ns}$ were $-30°$, $-40°$.

uncertainty. At the lower latitudes where it is likely that $|s_{\rm ns} - {\rm Lat}| < \pi/2$, the effect of the north-south slope is to make $|\Psi| > |s_{\rm ew}|$. It is useful to compare Ψ to the total slope angle Θ, where

$$\cos|\Theta| = \cos|s_{\rm ew}|\cos(s_{\rm ns}). \qquad (13)$$

Using the fact that $\sin|\Theta| < \sin|s_{\rm ew}|$ we see that

$$\tan|s_{\rm ew}| < \tan|\Psi| < \tan|\Theta|, \qquad (14)$$

so that the angle Ψ provides an estimate of the field line slope that is bracketed by the east-west slope and the total slope and whose sign gives the correct sense of the east-west direction. Thus, the observationally accessible tilt angle Ψ does not correspond to an angle relating the magnetic field to a coordinate system but does provide a constrained estimate of the magnetic field slope. These properties need to be taken into account when interpreting the tilt maps prepared with the method of the preceding section. The lines where $\Psi = 0$ correspond to loci where the east-west field component is zero and the field is in the meridional plane rather than loci where the field is vertical. Consequently, we will refer to regions where the tilt angle Ψ is small as having a meridional magnetic field and the loci of $\Psi = 0$ as the meridional neutral lines.

7. SYNOPTIC CHARTS

The application of the above methods produces synoptic charts showing the B_v magnetic field strength, the locations of the neutral lines, and maps of the magnetic field's east-west tilt. These maps can be projected onto a sphere and viewed from a direction appropriate to any time during the rotation. This reprojected image is different from any real image because it has had the effect of the magnetic field line tilt removed. For example, an apparent neutral line position when determined from a longitudinal Zeeman effect magnetograph will come at the point where the field lines are perpendicular to the line of sight. When a curved field line, such as is part of an arch, is observed at a position east or west of the central meridian, this point of orthogonality will be displaced toward the central meridian by an amount that depends on the radius of curvature of the arch. The position for the neutral line derived following the method in the preceding section is not sensitive to this effect. As a sample of the output of the method, the double charts in Figures 9, 10, and 11 show the results for three successive Carrington rotations in 1999. The upper part of each figure gives B_v color coded so that red is negative and blue is positive, along with the comparison positions of the prominences as determined by Mouradian (1998a, 1998b) shown as the solid green bars

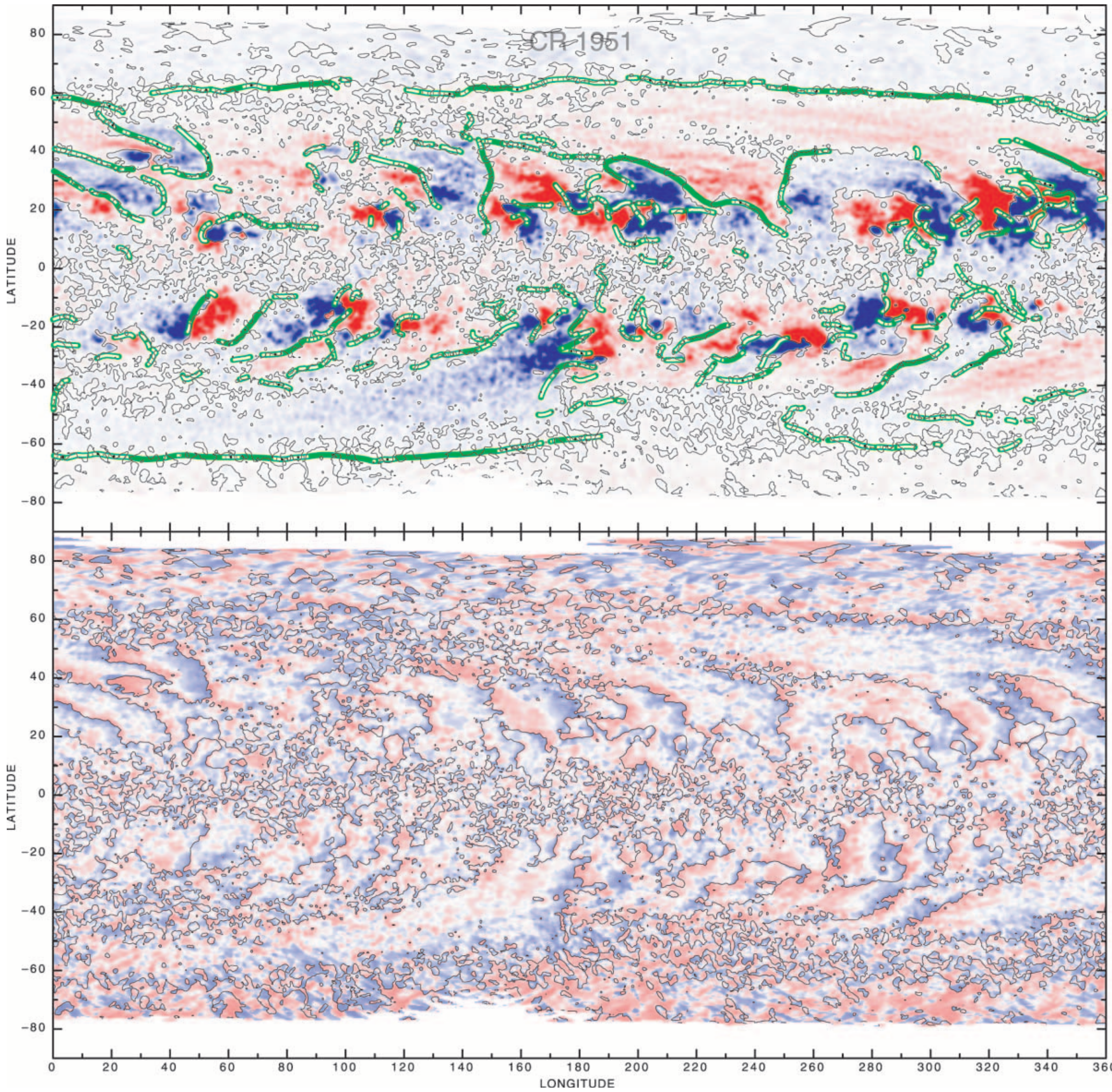

FIG. 9.—This figure shows solar magnetic fields in a synoptic chart format for Carrington rotation 1951 (1999 June 24 to July 21). The top panel gives the zero magnetic field lines with the field polarity and field strength as indicated by the red/blue colors overlaid with the filament locations from the Meudon synoptic chart for this rotation (Mouradian 1998a, 1998b). The lower panel gives the slope angle of the magnetic field lines in an east-west direction. For the slope angle map, the sign of the direction of the field vector is ignored so that the figure shows the angle between the local meridional plane and the plane containing the field line. Tilts toward the east (i.e., the upper part of the field line is east of the lower part of the field line) are shown as red while tilts to toward the west are shown as blue. A meridional neutral line with $\Psi = 0$ is white while a horizontal field line is either saturated red or blue.

and the green bars with central white or white and black lines. The positions of the polar crown filaments are in good agreement between these two data sets. Snodgrass et al. (2000) have also used the Mount Wilson data to study the polarity reversal during solar cycle 22 and found that there was good agreement between filament positions and the magnetic neutral lines.

The tilt maps in the lower parts of each figure provide new information concerning the magnetic field structure near the neutral lines. There is naturally a point of zero slope between the east-leaning regions and the west-leaning regions, and this point corresponds to a neutral line. The new information comes from the size of the region where the field lines are significantly tilted. The areas between relatively oppositely polarized, weakly magnetized active regions tend to have large sections where the field is not vertical. In some cases with strong fields on both sides of the meridional neutral line, the tilt remains small nearby, whereas for other cases the tilt becomes large in the adjacent regions. Also, for the crown filament regions, the tilt remains direct; i.e., it slopes from lower east to upper west for points to the east of the neutral line and the opposite for points to the west of the line. The model of Martin & Echols (1994) suggests that differential rotation might have reversed the sense of this orientation. Comparison of the tilts in successive rotations shows that this parameter is stably determined by the analysis method we have used and that the differences between structures of different regions are of solar origin. Detailed modeling of the configuration is required to determine the implications of the various geometric patterns.

The characteristic of the Mount Wilson system wherein several spectral line components are measured exactly simultaneously presents a new opportunity for studying solar currents and one component of the Lorentz force. As seen above, the geometric analysis is able to obtain the

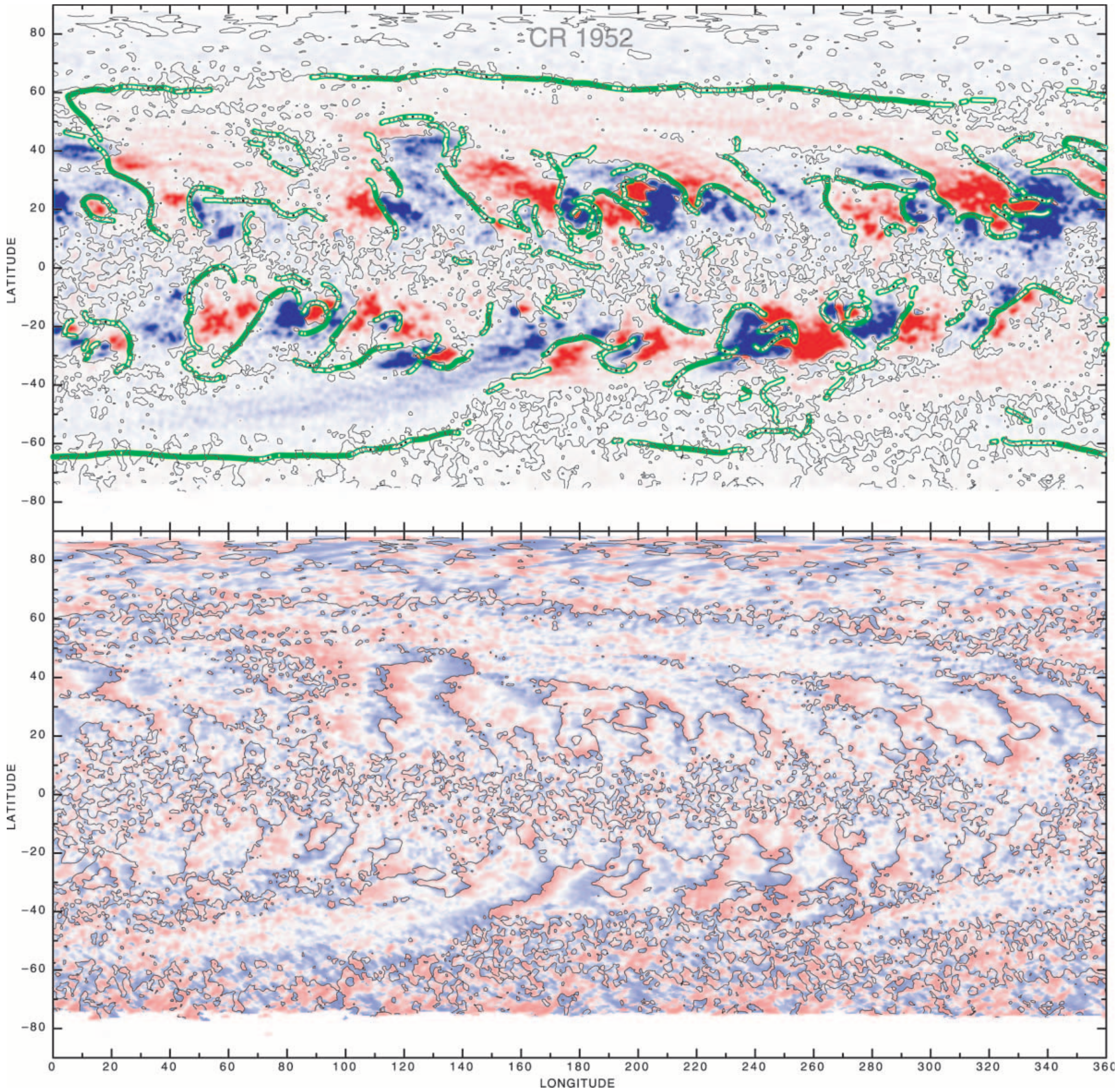

FIG. 10.—Synoptic charts for Carrington rotation 1952 in the same format as Fig. 9

slowly evolving part of the east-west component of the magnetic field without being influenced by the uncertainty in the north-south tilt angle. The level of photon noise in the magnetic field measurement is very small, and the dominant noise comes from the effects of seeing fluctuations. The simultaneous acquisition of measurements from several spectral line samples at different solar altitudes means that differences between these samples should cancel out the effects of atmospheric seeing and leave us with a measurement influenced only by photon noise. Consequently, we may be able to obtain a measure of the north-south component of $\nabla \times \boldsymbol{B}$, which in turn may be related to the north-south electric current and the east-west Lorentz force. A calibration and reduction of the additional spectral line sample pairs is under way will be the subject of future publications.

8. THE FLARE OF 2000 JULY 14

An example of an event that released a strong outburst of energetic protons is the flare of 2000 July 14, commonly referred to as the Bastille Day flare of 2000. An application of the above techniques to the analysis of the slowly evolving part of the magnetic field is given in Figure 12. The upper set of three figures gives the magnetic field results extracted from the synoptic map for the Carrington rotation centered on the time of the flare. As described above, the magnetic neutral lines as well as the field tilts are derived from all available observations of the part of the solar surface where the flare occurred. These rectangles were then cropped out of the average images. The right figure is the superposition of the magnetic neutral lines onto the final image from gif animation of EIT 195 Å images.[2] The final image from this sequence taken at 12:25 UT on 2000 July 14 was extracted and overlain with the neutral lines from the full disk image used in the two upper left boxes. The coalignment was carried out by fitting the limb of the neutral line image to the apparent limb in the EIT image. The lower three images were extracted from single Mount Wilson synoptic program magnetograms.

[2] These can be found at http://science.nasa.gov/headlines/images/radiationstorm/flare_eit195_big.gif.

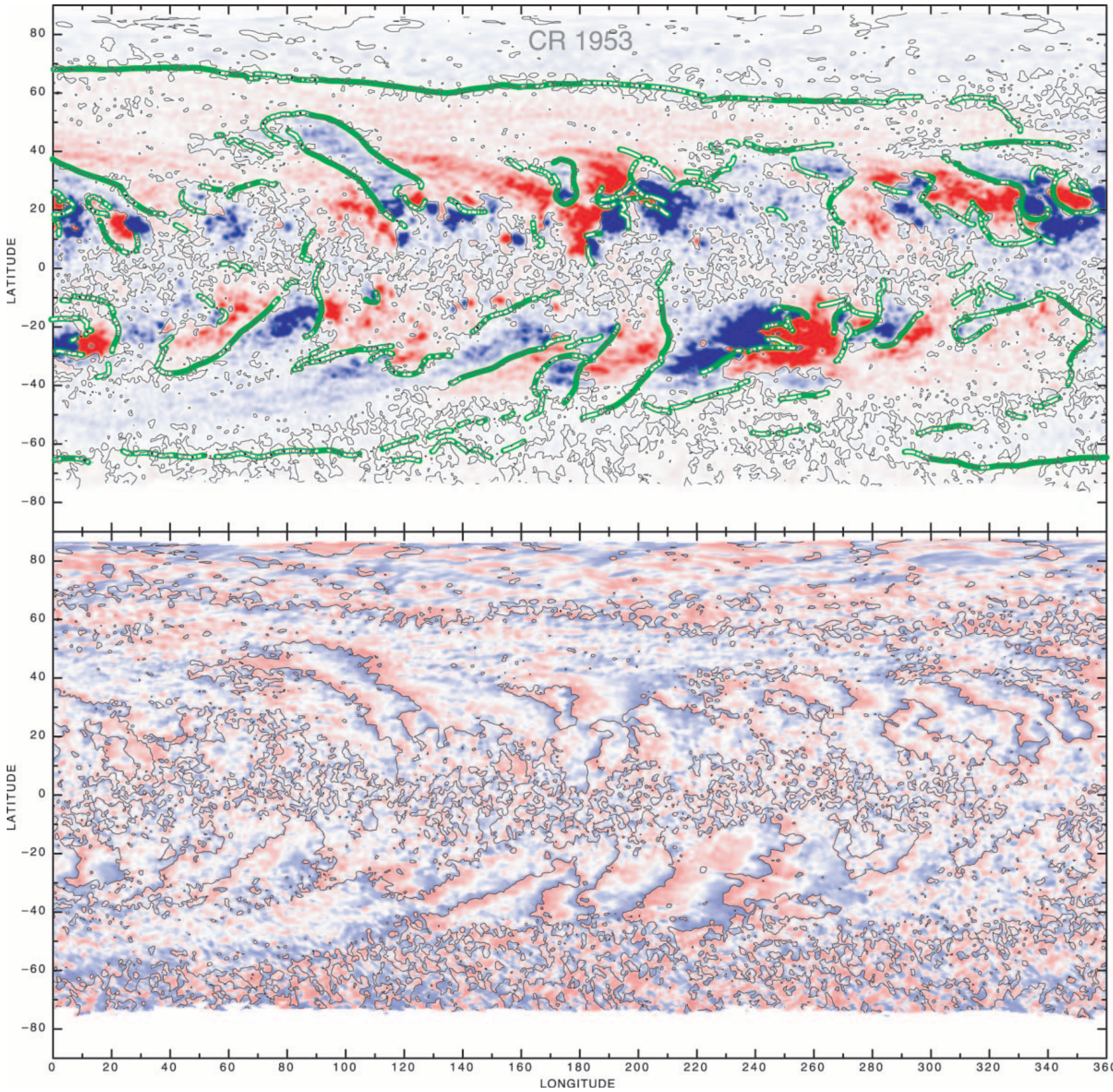

FIG. 11.—Synoptic charts for Carrington rotation 1953 in the same format as Fig. 9

Based on the information available from the two new images derived from the analysis given here, we are able to offer some physical interpretation of the state of the region through the flare event. An arcade or arch structure consists of magnetic field lines sloping from lower left toward upper right with a neutral line at the point where the blue color is strongest. Further to the right the arch structure slopes from upper left toward lower right moving away from the neutral line. This pattern is evident in the lower right corner of the tilt map in Figure 12. In a case with nothing but a current sheet, the field line slopes are small up until the meridional neutral line. A configuration approaching this pattern is seen on the upper left of the tilt map where the slopes are small just to the right of the meridional neutral line but are sloping lower left to upper right on both sides of this low slope zone. The meridional neutral lines along which the Bastille Day flare occurred are mostly in an east-west direction in agreement with the configuration observed during the flare itself. Interestingly, the tilt along this line indicates that the field was sheared in such a way that the configuration could have been produced if the region to the north of the flaring meridional neutral line was drifting from left to right relative to the region to the south. Shear indicating the same direction of drift is seen along the meridional neutral line north of the flaring zone. This suggests that the blue polarity fields were drifting westward relative to the red polarity fields. In addition, the time sequence along the strip below in Figure 12 shows the intrusion of a red polarity zone into the blue polarity region. This intrusion was gone on July 14 after the flare had ended. The intrusion is consistent with the idea that the opposing polarity regions were moving into the region during this period possibly due to the twisting associated with the α effect of the dynamo process. It is clear from the sequence of changes shown here that the tilt-map approach is capable of revealing information about the active regions that would otherwise be available only from vector magnetograph studies.

9. POLAR FIELD REVERSAL AND THE GLOBAL BIPOLAR MAGNETIC FIELD DISTRIBUTION

One of the primary objectives of synoptic solar programs is to improve our understanding of the solar dynamo process. We can observe the Sun every clear day and build up a

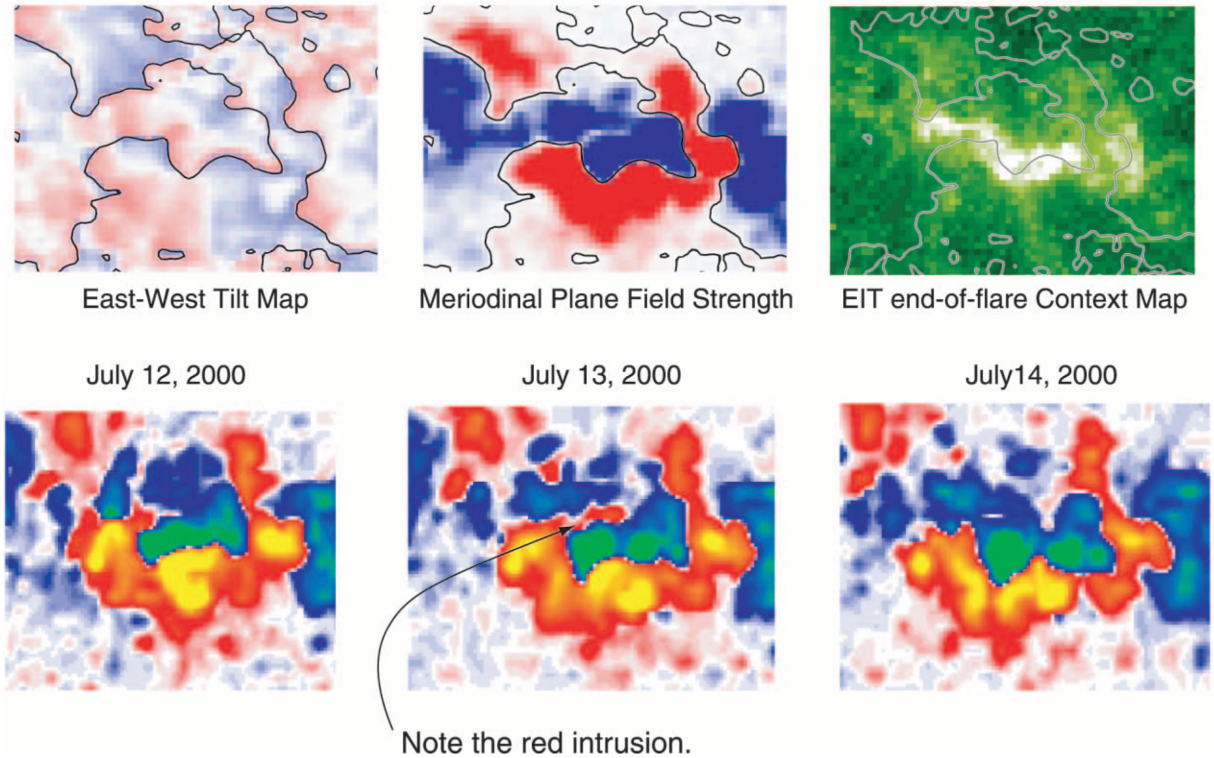

FIG. 12.—This figure shows the deduced long-time average magnetic field configuration deduced from all available observations for the rotation during which occurred the 2000 July 14 flare, commonly referred to as the Bastille Day Flare of 2000. The synoptic surface was then rotated so that the subsolar point at the time of the flare is at disk center. The Shrauner-Scherrer method produces two magnetic field components—one is in the east-west direction and the other is in the meriodinal plane that passes through the Sun's rotation axis and the point on the solar surface. The tilt map on the left gives the east-west angle of the field lines. The color code is independent of which direction on the field lines the arrow points and is such that a blue region slopes from lower left to upper right while a red region slopes from lower right to upper left. The lower three figures track the flare-producing active region and were extracted from the daily magnetogram observations of the 150 foot tower.

record of the detailed evolution of the magnetic field configuration. Butterfly diagrams of magnetic flux are a common way of studying the large-scale evolution of the Sun's magnetism. In such a diagram, the flux is averaged over a full rotation and plotted as a function of the mid-time of the rotation and latitude (Harvey 1992; Ulrich 1993). This format permits a highly condensed summary of the evolution but obscures the presence and structure of active longitudes or nests of solar activity. The other common format for presentation of solar magnetism is the synoptic chart. This allows a detailed examination of the location and strength of the magnetic fields and shows clearly the location and structure of individual active regions. The individual synoptic chart does not permit an easy examination of the long-term trends in active region structure because the detail is spread out over too large a format to be viewed as a whole. In order to bridge two timescales, Ulrich (1993, 1998) introduced a representation called a supersynoptic chart in which each synoptic chart is highly compressed in longitude and plotted with zero longitude on the right and 360° longitude on the left. Many such charts can be plotted next to each other to form a supersynoptic chart. Depending on the length of time to be displayed, detail within each rotation can be retained while still permitting overall trends to be seen. Figure 13 gives a current example of a supersynoptic chart extending from the time of solar minimum between cycles 22 and 23 up to the time of polarity reversal in early 2001.

The supersynoptic chart shows that just after solar minimum, the new active regions have their two polarity components lined up closely in latitude. As the differential rotation and convection breaks up and diffuses the decaying parts of both polarities, the result largely cancels. Later in the cycle, the Joy's law displacement of the trailing spot poleward also extends to the broader associated plage regions. As this change develops, the dispersal of the decaying active regions is altered because the trailing polarity starts from a poleward position. Consequently, as it is dispersed its polarity tends to dominate. This effect begins by the formation of feather-like plumes that move toward the opposing polar regions but are not able to penetrate. This behavior is strikingly evident from 1998 to 2000. By mid 2000, the active regions have gone beyond being slightly twisted and frequently have their neutral lines running largely east-west with the trailing spot polarity completely dominating. At this time the trailing spot polarity merges around the solar circumference at the higher latitude so that when meridional circulation brings it to the pole, the reversal can take place. A long-recognized (Babcock 1961) key question is then to find the cause of the increasing poleward displacement of the trailing spot polarity as the cycle progresses. The period during 1999 is shown in an expanded format in Figure 14.

Beginning with the earliest solar cycle models (Parker 1955) the role of bipolar magnetic regions (BMRs) and the tilt of their centers relative to the Sun's equator has been an essential ingredient. The concept is that cyclonic motions due to rising and diverging flows are part of the process that brings a section of the toroidal flux tube to the surface. Parker (1955) demonstrated that a distribution of small BMRs can interact to yield a large-scale dipole field. The α-

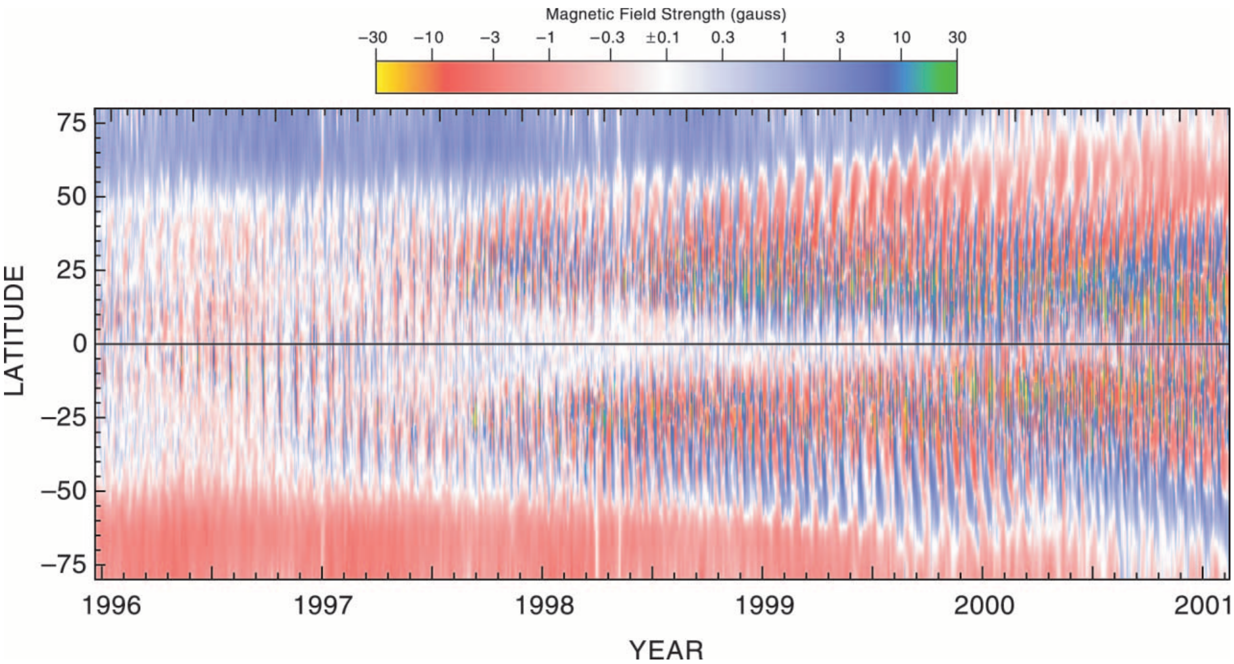

FIG. 13.—This figure is a supersynoptic chart formed from the magnetic data beginning at the most recent solar minimum in 1996 and extending to the early part of 2001 when the polarity reversal is in progress. A supersynoptic chart is created by compressing each synoptic chart, reversing the sign of the horizontal axis so solar longitude runs backward, and abutting successive charts to one another. This creates a plot in which time running forward corresponds to the successive passage of points past the apparent solar central meridian. Time is indicated on the bottom axis and successive Carrington rotation boundaries are indicated on the top axis. The long-term trends of the solar cycle are often presented in a similar fashion but with the longitudinal structure averaged out. The format here allows the simultaneous evaluation of long-term trends in latitudinal structure. The color scale is proportional to log $|B|$ and is given on the color bar above the diagram.

ω models similarly treat the conversion of the toroidal field to a poloidal field as a statistical process involving a distribution of BMRs. The explicit testing of the model is difficult because it requires the identification of the BMRs, a determination of the boundaries of each, and the location of centroids of regions of opposing polarity so that a tilt angle can be measured. An approach of this type has been discussed by Wang & Sheeley (1991) and Howard (1993), and the role of ephemeral regions has been discussed by Harvey (1994). These studies have measured the BMR tilts and concluded that they are in quantitative agreement with the requirements of the model.

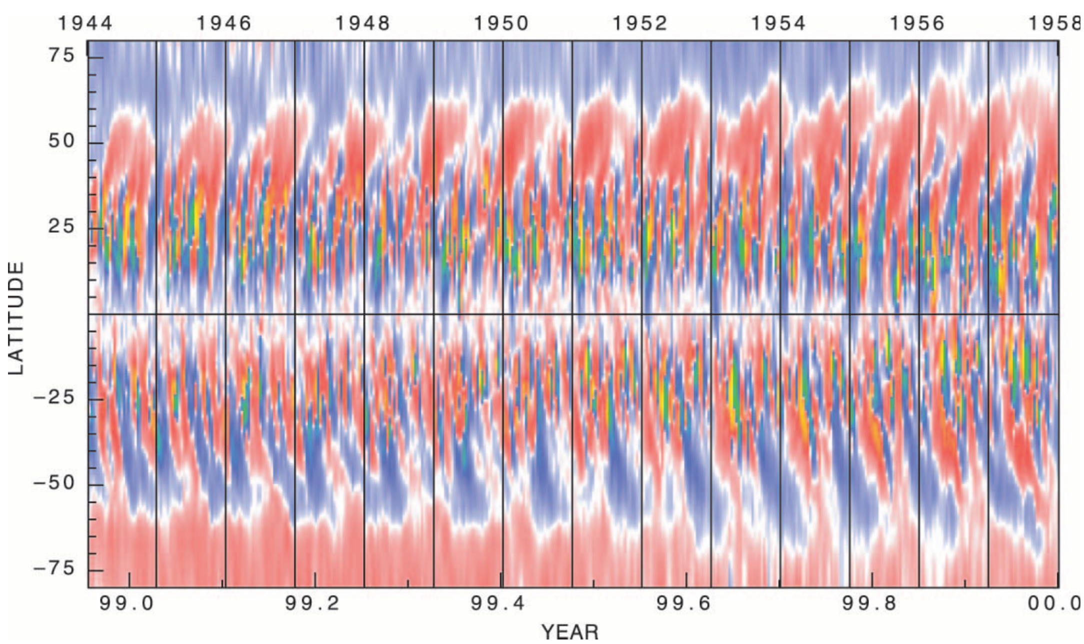

FIG. 14.—This is an expanded section of the supersynoptic chart shown in Fig. 13 showing the interesting period of 1999 when the bipolar magnetic regions began their shift toward having the trailing polarity located poleward of the leading polarity. The color coding is the same as in Fig. 13. In addition, the boundaries of the Carrington rotations are indicated here since the degree of compression along the time axis is less than in Fig. 13.

The focus by the above studies on identified regions to determine which plays the greatest role in reversing the Sun's magnetic dipole raises the possibility that the details of the selection and measurement could influence the conclusions. In particular, Wang & Sheeley (1991) conclude that the process proceeds at a rate that is largely independent of the phase of the solar cycle. Figure 13 suggests, however, that the development of the reversing dipole strength might be of sufficiently large scale that the demarcation of the BMRs and the determination of a tilt angle might not capture the full process. The question in fact is not to measure a tilt of a particular region but rather to determine when a bias develops that causes the trailing polarities of the BMRs to be closer on average to the poles than is the leading polarity. The product of the signed magnetic field and the latitude is a measure of the BMR tilt, which can be averaged over the whole solar surface without the need to identify specific active regions—if trailing polarities are positive in the northern hemisphere and negative in the southern hemisphere, the product will be positive in both hemispheres as long as the trailing polarity is closer to each pole. When carried out over the full solar surface, however, this net poleward bias is in fact exactly the dipole moment of the magnetic field. Thus, this approach to a global measure of the BMR tilt results instead in the calculation of the total dipole moment. In order to arrive at a useful global measure of BMR tilt, we need another indicator that is sensitive to the difference between the contribution of the BMRs and that from the broadly distributed dipole structure that is dominated by the polar magnetic fields during sunspot minimum period. The remainder of this section demonstrates a method of making this distinction on the basis of the latitudinal field structure. As a preliminary, we review the calculation of the dipole moment, since it is essential to distinguish between this quantity and a global measure of the BMR tilt.

We can define a longitude-dependent contribution function for the dipole moment using the data format of the supersynoptic chart. The solar surface in this format is divided into a series of longitude strips $\delta\phi$ wide that run from pole to pole. The contribution of each longitude strip to the axial dipole moment, $\delta B_{\rm Dipole}$, can be calculated by applying the same latitude-dependent projection factor to the line-of-sight magnetic field as is used to calculate the axial dipole moment of the full surface. Following Hoeksema (1984) we take the measure of the dipole moment to be the coefficient g_{10}, which multiplies the associated Legendre polynomial $P_l^m[\cos(\theta)]$, where θ is the colatitude. If each longitudinal strip were to extend over the full circumference, we could extract the value of g_{10} from

$$g_{10} \approx \frac{3}{2}\int_{-1}^{1} \cos(\theta) B_r \, d\cos(\theta) \qquad (15)$$

based on the fact that the associated Legendre polynomials are orthogonal and $P_1^0 = \cos(\theta)$. Since the field does depend on longitude, we use a different symbol for this integral: $b_{\rm Dipole}$. For this calculation we take the surface field to be vertical in the north-south direction and correct the field for the saturation effect, ϵ, so we use

$$B_r = \epsilon^{-1} B_{\rm Observed} / \sin(\theta) \ . \qquad (16)$$

In our supersynoptic format the data are averaged into 34 bins of equal size in $\cos(\theta)$ so that we calculate the dipole contribution from

$$b_{\rm Dipole} = \frac{3}{34}\sum_{i=1}^{34} \epsilon^{-1} B_{\rm Observed} \frac{\cos(\theta)}{\sin(\theta)} \ . \qquad (17)$$

When this function is averaged over longitude, we recover the global dipole moment while by retaining the longitude dependent part we obtain additional measures of the global field.

We seek a quantity that distinguishes the dipole contribution of the BMRs from the global field. A general field gives a steady but nonzero value for $b_{\rm Dipole}$, whereas bipolar regions produce large fluctuations in this function: each longitude strip passes first through the leading polarity and then passes through the following polarity. Thus, the passage of a BMR is represented through a large swing in the longitude-dependent contribution function. Thus, we can measure the strength of the BMRs by calculating the variance of $b_{\rm Dipole}$ defined as $\delta b_2 = \delta b_{\rm Dipole}^2 = (b_{\rm Dipole} - \langle b_{\rm Dipole}\rangle)^2$, where the angular brackets indicate a smoothing operation. The smoothed value of this variance is an indicator of the strength of the solar cycle. (Here and below the smoothing operation involves the convolution of a quantity with a Gaussian having a width parameter equal to 1.4 Carrington rotations.)

Furthermore, if the bipolar region is tilted, it will produce an average of $b_{\rm Dipole}$ that favors the spot that is closer to the pole. The swing of $\delta b_{\rm Dipole}$ associated with the tilted BMR is then not symmetric about zero and the $\delta b_{\rm Dipole}$ distribution is skewed. The skewness that is the average of the cube of $\delta b_{\rm Dipole}$ provides the measure we seek. Note that the skewness is the product of two indicators, the dipole moment contribution and the variance that is the strength indicator. We define $\delta b_3 = \delta b_{\rm Dipole}^3$ to be the skewness indicator. Thus, we see that we can form three measures of the dipole moment: first is the smoothed version of the dipole moment, $\langle b_{\rm Dipole}\rangle$; second is the smoothed squared deviation or variance, $\langle \delta b_2\rangle$; and third is the cubed deviation or skewness, $\langle \delta b_3\rangle$. If the tilt of the BMRs is the cause of the reversal of the general dipole field, there should be a correspondence between $\langle \delta b_3\rangle$ and the time derivative of the dipole field $\langle b_{\rm Dipole}\rangle$.

The time dependence of the dipole moment and the above three quantities derived from dipole moment contribution functions are shown in Figures 15 and 16. Note that these Figures are based on the Mount Wilson 150 foot tower record starting in 1986 rather than the more limited period used in Figure 13. The first two panels, *a* and *b*, give the values of $b_{\rm Dipole}$ derived from northern hemisphere alone using the magnetic field without the ϵ^{-1} factor. These quantities can be compared directly to the plots of Figures 13 and 14. Subpanel *c* on the upper right shows the corrected dipole moment including both hemispheres along with the smoothed result for the corrected dipole moment. Shown on this diagram is the axial dipole moment from the Wilcox Solar Observatory (WSO) that has been corrected for the line-of-sight projection factor but not a saturation factor. The larger dipole moment from MWO relative to those from WSO is likely the result of a combination of the saturation effect and the effect of the greater spatial resolution from the MWO system. It is interesting that the net polarity is relatively constant through the declining phase of cycle 22 and does not begin to change substantially until about 2

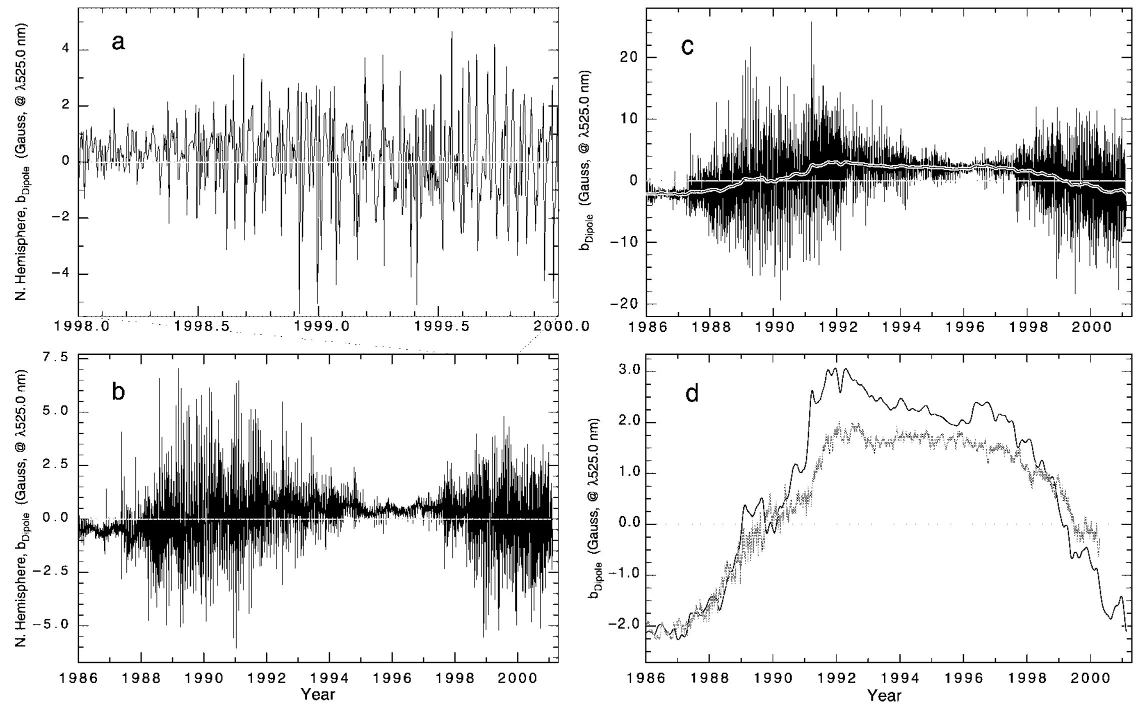

FIG. 15.—This figure gives the projected contribution of each longitude strip to the solar dipole moment. The period covered is longer than is shown on Fig. 13 and includes all data since the beginning of the period when multiple observations per day were acquired. Panels *a* and *b* give the projected solar dipole moment from the northern hemisphere alone using the line-of-sight field without correction for the latitude-dependent saturation factor and without correction for an assumed vertical orientation along the north-south direction. Both of the corrections have been applied in plot *c*, which shows the net dipole moment from both hemispheres along with the result of smoothing with a Gaussian having a width parameter equal to 1.4 Carrington rotations. Panel *d* compares the smoothed dipole moment from the MWO observations (*solid black line*) to the evolution of the dipole moment measured by the Wilcox Solar Observatory (Hoeksema 1992; the WSO data is plotted as the gray line). The lower dipole strength of the WSO results may indicate the need for applying a line saturation factor to the WSO data.

years after solar minimum. The final panel, *d*, on the right of Figure 15 shows the values of $\delta b_{\rm Dipole}$. Figure 16 shows the smoothed skewness $\langle \delta b_3 \rangle$ along with the smoothed time derivative of $d\langle b_{\rm Dipole}\rangle/dt$. We note several points from Figures 15 and 16:

1. The strong and tilted BMR in the northern hemisphere at almost exactly 1999.0 has an effect on the global pattern of dipole moment that shows up as a series of three rotations where there is strong negative bias to the dipole moment. These three excursions are larger than the adjacent amplitude and mark the start of the vigorous polarity reversal process.

2. The dipole moments calculated from MWO and WSO data are in good overall agreement apart from a multiplicative factor of about 1.3–1.5. The MWO trend is somewhat more variable than that of the WSO data, and this may be a result of the higher spatial resolution, which responds to more localized features.

3. The most important result is shown in Figure 16, which shows the smoothed skewness, $\langle \delta b_3 \rangle$, and the smoothed time derivative of the dipole moment. The measurement of the skewness is not subject to error at a level that would influence this plot—the irregularity shown comes from the field distribution on the Sun and not from an uncertainty in the measurement. The correspondence between the skewness and the temporal derivative, while not exact, nonetheless suggests that we may be able to identify the skewness as being the source of the changes in the Sun's dipole moment. This is in agreement with the generally accepted model of the solar cycle, which postulates that the α effect twists the field lines to convert a toroidal field into a dipole field. The strong variation in $\langle \delta b_3 \rangle$ is significant and shows that the process is dominated by large scale components. Of particular interest is the very large burst of skewness at the beginning of 1991 that produces a spurt in the growth of the strength of the solar cycle that had previously appeared to be near its maximum. The smaller skewness bursts from the end of 1998 to the beginning of 1999 are also associated with a strengthening of the cycle.

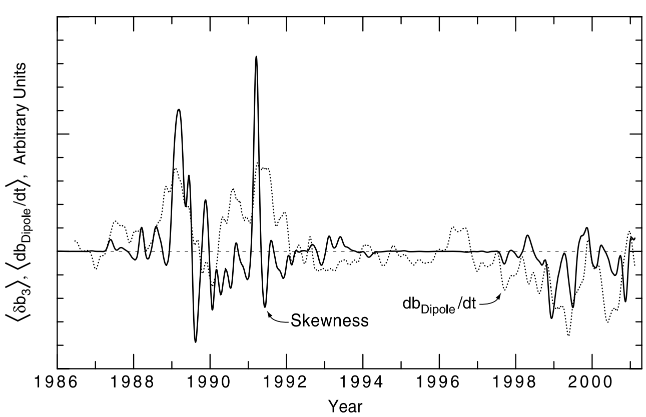

FIG. 16.—This figure compares time dependence of the dipole skewness $\langle \delta b_3 \rangle$ shown as the solid line to the time derivative of the dipole moment $d\langle b_{\rm Dipole}\rangle/dt$ shown as the dotted line.

When treated from this global approach, it is evident that the polarity reversal process is quite irregular in its progression. The reversal of the Sun's dipole moment appears to be the result of the skewness bursts that are of very large spatial scale and that come at distinct points in the solar cycle. The temporal distinctness and global spatial scale of these events suggest that a numerical modeling approach to their study may be advantageous.

10. CONCLUSIONS

This paper has presented a set of improvements in the data acquisition and analysis system in use for the synoptic program at the 150 foot tower telescope on Mount Wilson along with two new applications. The instrument changes permit the acquisition of data from four spectral lines simultaneously. The data analysis is improved through the treatment of saturation effects in the different spectral lines. The new analysis approach determines the position of neutral magnetic lines on the solar surface along with the east-west magnetic line tilt. A display of the neutral line and magnetic tilt in a typical set of three Carrington rotations shows that the neutral line position determination is in good agreement with the observed locations of quiescent prominences, including the polar crown filament, and that the magnetic line tilt is stable from one rotation to the next. Furthermore, the application of the method to the magnetic region associated with the flare of 2000 July 14 reveals evidence of a systematic shear in the region of the flaring. The second new application starts with a new presentation of long-term trends in magnetic field evolution in a format we refer to as a supersynoptic chart. Examination of this presentation suggests that the bipolar magnetic region tilt, which plays a critical role in dynamo models, occurs in the form of distinct large-scale episodes where major BMRs have a tilt along the lines of Joy's law for sunspots. A quantitative method of measuring the global bias of the BMR magnetic fields is presented. The skewness in the distribution of dipole moment contributions as a function of longitude is shown to be a good measure of the BMR tilt, which, according to dynamo models, should be related to the reversal of the dipole moment. This skewness and the time derivative of the overall dipole moment show similar behavior confirming that the Parker, Babcock model for the dynamo is essentially correct. The analysis here shows that rather than coming as a nearly continuous sequence of small dipole contributions, the dipole skewness comes as a small number of burstlike events.

The irregularity in the temporal behavior of the skewness suggests the possibility that a large-scale instability could be at work. It has been found by Longcope & Klapper (1997) that helicity in subphotospheric flux tubes can produce the observed tilt associated with Joy's law. Differential rotation applied to flux tubes that span a wide latitude range can produce this helicity. When the total twist of a tube exceeds a critical value, the tube becomes unstable to a kink deformation (see Priest 1984, § 7.4.1 for discussion of this process). Although the analysis is done in a more idealized model than can be applied to the Sun, the onset of the instability may depend on the local rate of differential rotation. This idea could help explain a puzzle of the solar cycle, which is the correspondence between the zone of maximum shear and the location of active regions first noted by Snodgrass (1987). This phenomenon is part of the process known as the torsional oscillations (Howard & LaBonte 1980; LaBonte & Howard 1982; Snodgrass & Howard 1984; Ulrich 2001). As is seen clearly in Figure 1 of Ulrich (2001), during the period near the beginning of each cycle, the magnetic regions are found only poleward of the zone of maximum shear. Since this enhancement of shear increases the rate of twist in the flux tubes, it could trigger a kink instability. There is no evidence, however, that the torsional oscillations extend more deeply than the outer 5% of the solar radius (Howe, Komm, & Hill 2000; Toomre et al. 2000).

Future applications of the system at the 150 foot tower will include the intercomparison of magnetic fields measured with different systems including MDI on *SOHO*. Another important application will be the comparison of the magnetic field at different altitudes in the solar atmosphere through the use of the Na D_1 line.

This work has been supported over a period of 15 years by several different grants from NASA, NSF, and ONR. We thank Nick Magnone for his skillful construction of the housing and stage components of the 24-channel photomultiplier system. We thank referee Harrision Jones for his thoughtful reading of this paper and helpful comments that corrected several errors in the original manuscript. We also thank Luca Bertello for his comments on a draft of this paper and for providing calculations of the contribution functions shown in Figure 4, as well as Sarah Lipscy for a careful reading of the manuscript.

REFERENCES

Altschuler, M. D., & Newkirk, G., Jr. 1969, Sol. Phys., 9, 131
Arge, C. N., & Pizzo, V. J. 2000, J. Geophys. Res., 105, 10465
Babcock, H. W. 1961, ApJ, 133, 572
Caccin, B., Gomez, M. T., Marmolino, C., & Severino, G. 1977, A&A, 54, 227
Charbonneau, P., & MacGregor, K. B. 1997, ApJ, 486, 502
Dikpati, M., & Charbonneau, P. 1999, ApJ, 518, 508
Frazier, E. N., & Stenflo, J. O. 1972, Sol. Phys., 27, 330
Gabriel, A. H., et al. 1995, Sol. Phys., 162, 61
Gilman, P. A. 2000, Sol. Phys., 192, 27
Gilman, P., & Howard, R. 1986, ApJ, 303, 480
Hagyard, M. J. 1987, Sol. Phys., 107, 239
Hagyard, M. J., Smith, J. B., Jr., Teuber, D., & West, E. A. 1984, Sol. Phys., 91, 115
Harvey, K. L. 1992, in Proc. NSO Sac Peak 12th Summer Workshop, The Solar Cycle, ed. K. L. Harvey (ASP Conf. Ser. 27; San Francisco: ASP), 335
———. 1994, in Solar Surface Magnetism, ed. R. J. Rutten & C. J. Schrijver (Dordrecht: Kluwer), 347
Hirayama, T. 1985, Sol. Phys., 100, 415
Hoeksema, J. T. 1984, Ph.D. thesis, Stanford Univ., CSSA Rep. 7
Hoeksema, J. T. 1992, in Solar Wind Seven, ed. E. Marsch & R. Schwenn (Oxford: Pergamon), 191
Howard, R. F. 1974, Sol. Phys., 39, 275
———. 1991, Sol. Phys., 134, 233
———. 1993, Sol. Phys., 145, 105
———. 1994, in Solar Surface Magnetism, ed. R. J. Rutten & C. J. Schrijver (Dordrecht: Kluwer), 297
Howard, R., Boyden, J. E., Bruning, D. H., Clark, M. K., Crist, H. W., & LaBonte, B. J. 1983, Sol. Phys., 87, 195
Howard, R., & LaBonte, B. J. 1980, ApJ, 239, L33
Howard, R. F., & Stanchfield, D. C. H., II. 1995, Sol. Phys., 156, 29
Howard, R., & Stenflo, J. O. 1972, Sol. Phys., 22, 402
Howe, R., Komm, R., & Hill, F. 2000, Sol. Phys., 192, 427
Hoyng, P. 1994, in Solar Surface Magnetism, ed. R. J. Rutten & C. J. Schrijver (Dordrecht: Kluwer), 387
Keller, C. U. 1993, in IAU Colloq. 141, The Magnetic and Velocity Fields of Solar Active Regions, ed. H. Zirin, G. Ai, & H. Wang (ASP Conf. Ser. 46; San Francisco: ASP), 3
Krause, F., & Rädler, K.-H. 1980, Mean Field Magnetohydrodynamics and Dynamo Theory (Oxford: Pergamon)
Kuperus, M., & Tandberg-Hanssen, E. 1967, Sol. Phys., 2, 39

LaBonte, B. J., & Howard, R. 1982, Sol. Phys., 80, 361
Leighton, R. B. 1969, ApJ, 156, 1
Lites, B. W., et al. 1995, ApJ, 446, 877
Longcope, D. W., & Klapper, I. 1997, ApJ, 488, 443
Markiel, J. A., & Thomas, J. H. 1999, ApJ, 523, 827
Martin, S. F., & Echols, C. R. 1994, in Solar Surface Magnetism, ed. R. J. Rutten & C. J. Schrijver (Dordrecht: Kluwer), 339
Mickey, D. L. 1985, Sol. Phys., 97, 223
Minnaert, M. G. J. 1946, MNRAS, 106, 98
Mouradian, Z. 1998a, in Proc. 18th NSO/Solar Peak Summer Workshop, Synoptic Solar Physics, ed. K. S. Balasubramaniam, J. W. Harvey & D. M. Rabin (ASP Conf. Ser. 140; San Francisco: ASP), 197
Mouradian, Z. 1998b, in Proc. 18th NSO/Solar Peak Summer Workshop, Synoptic Solar Physics, ed. K. S. Balasubramaniam, J. W. Harvey, & D. M. Rabin (ASP Conf. Ser. 140; San Francisco: ASP), 181
Parker, E. N. 1955, ApJ, 122, 293
———. 1993, ApJ, 408, 707
Priest, E. R. 1984, Solar Magnetohydrodynamics (Boston: Reidel)
Rüdiger, G., & Brandenburg, A. 1995, A&A, 296, 557
Scherrer, P. H., et al. 1995, Sol. Phys., 162, 129
Shrauner, J. A., & Scherrer, P. H. 1994, Sol. Phys., 153, 131
Snodgrass, H. B. 1987, Sol. Phys., 110, 35
Snodgrass, H. B., & Howard, R. 1984, ApJ, 284, 848
Snodgrass, H. B., Kress, J. M., & Wilson, P. R. 2000, Sol. Phys., 191, 1
Spruit, H. C., Schüssler, M., & Solanki, S. K. 1991, in Solar Interior and Atmosphere, ed. A. N. Cox, W. C. Livingston, & M. S. Matthews (Tucson: Univ. Arizona Press), 890
Steenbeck, M., & Krause, F. 1969, Astron. Nachr., 291, 49
Steiner, O. 1994, in IAU Symp. 154, Infrared Solar Physics, ed. D. M. Rabin, J. T. Jefferies, & C. Lindsey (Dordrecht: Kluwer), 407
Steiner, O., & Pizzo, V. J. 1989, A&A, 211, 447
Stenflo, J. O. 1973, Sol. Phys., 32, 41
Toomre, J., et al. 2000, Sol. Phys., 192, 437
Ulrich, R. K. 1992, in Proc. 7th Cambridge Workshop, Cool Stars, Stellar Systems, and the Sun, ed. M. S. Giampappa & J.A. Bookbinder (ASP Conf. Ser. 26; San Francisco: ASP), 265
———. 1993, in IAU Colloq. 137, Inside the Stars, ed. W. W. Weiss & A. Baglin (ASP Conf. Ser. 40; San Francisco: ASP), 25
———. 1998, in IAU Symp. 185, New Eyes to See Inside the Sun and Stars: Pushing the Limits of Helio- and Asteroseismology with New Observations from the Ground and from Space, ed. F.-L. Deubner, J. Christensen-Dalsgaard, & D. Kurtz (Dordrecht: Kluwer), 453
———. 2001, ApJ, 560, 466
Wang, J., Shi, Z., Wang, H., & Lü, Y. 1996, ApJ, 456, 861
Wang, Y.-M., & Sheeley, N. R. 1990, ApJ, 355, 726
———. 1991, ApJ, 375, 761
———. 1992, ApJ, 392, 310
———. 1995a, ApJ, 447, L143
———. 1995b, ApJ, 449, L157
Wang, Y.-M., Sheeley, N. R., Jr., & Nash, A. G. 1991, ApJ, 383, 431
Zhao, X., & Hoeksema, J. T. 1993, Sol. Phys., 143, 41
———. 1995, J. Geophys. Res., 100, 19